STRAINED TWO DIMENSIONAL MATERIALS

By

Hiram Conley

Dissertation

Submitted to the Faculty of the

Graduate School of Vanderbilt University

in partial fulfillment of the requirements

for the degree of

DOCTOR IN PHILOSOPHY

in

PHYSICS

December, 2014

Nashville, Tennessee

Approved:

Professor Kirill Bolotin

Professor Richard Haglund

Professor Jason Valentine

Professor Sharron Weiss

ACKNOWLEDGMENTS

It takes many people to do all the work that is mentioned in this dissertation. Particular notice should be given to Nick Lavrik at Oak Ridge National Laboratory for his excellent help with the bimetallic cantilevers, especially his suggestion to use the silicon nitride platform which was much more successful than the gold graphene cantilevers that we had explored up to that point. I would also like to thank Jed Ziegler for allowing me to spend so much of his time measuring spectra of strained and unstrained MoS_2, Bin Wang and Yevgeniy Puzyrev for the computational help and willingness to answer an endless stream of questions, and Ryan Nicholl for helping get the final work of this thesis done. Also AKM Newaz, Dhiraj Prasai, Andrey Klots, and Alex Wynn who have been great group members to work with, solving countless problems together. Also I would like to thank Kirill Bolotin for never being content and always agitating for more.

ABSTRACT

Two dimensional materials are atomically or molecularly thin materials that extend macroscopically. In this dissertation we study optical and mechanical properties of these materials through controllable strain. The coefficient of thermal expansion of graphene is measured and shown to be negative, in agreement with predictions from soft condensed matter. Also the adhesion of graphene to a substrate is shown to be temperature dependent. Through strain engineering another two dimensional material, MoS_2, it is shown that its band gap is strain dependent. Strain transitions MoS_2 from a direct band gap to an indirect band gap material at strains of approximately 1.6%. Finally through strain engineering of another two-dimensional material, graphene, preliminary results suggest that it behaves as a two dimensional entropic spring, with an in-plane stiffness as low as 50 N/m.

TABLE OF CONTENTS

LIST OF FIGURES

CHAPTER I

Introduction

Condensed matter physics encompasses two broad fields, hard and soft condensed matter. Hard condensed matter physics focuses on 'hard' materials like metals and ceramics where the material properties are dominated by the crystal lattice of the material or electrons. The 'soft' materials studied in soft condensed matter are often polymers and biological systems that "that are easily deformed by thermal stresses or thermal fluctuations" as their physical behaviours "occur at an energy scale comparable with room temperature thermal energy[Wikipedia, 2014]." Soft materials manifest novel physical behaviours that are not predicted from atomic or molecular components but stem from the thermodynamics of the system.

By exploring the physical properties of two dimensional materials this dissertation straddles these two diverse branches of condensed matter physics. A typical hard condensed matter system is the crystal shown in figure I.1a while a prototypical soft condensed matter material is the lipid bilayer shown in figure I.1c. However if one has a crystal that has the thickness of a single atomic layer it is hard to know to which camp it belongs to. On the one hand it is crystalline and on the other hand thermal fluctuations can be dominate.

By probing the physical properties of these atomically thin, or two-dimensional, materials one can explore the interface of hard and soft condensed matter physics, where a materials properties can be dominated by the crystal lattice (as per hard condensed matter) or by its intrinsic size, and temperature (as per soft condensed matter). By exploring a material from both frames of reference one gains a more complete understanding of the material and enables one to engineer its material properties.

I.1 Two Dimensional Materials

Graphene has been the wunderkind of condensed matter physics due to its exceptional mechanical, electrical, and thermal properties. Graphene is the thinnest, strongest[Lee et al., 2008], most thermally conduc-

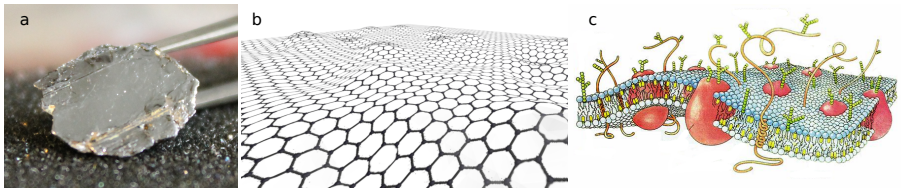

Figure I.1: Hard condensed matter is focused on hard, and generally crystalline materials like the crystal in a) while soft condensed matter physics is focused on soft systems like the lipid bilayer in b). Two dimensional materials are neither here nor there.

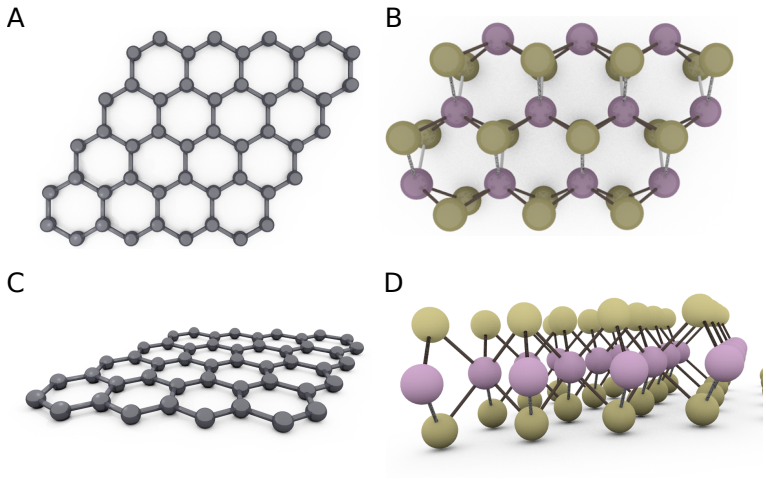

Figure I.2: Ball and stick representation of graphene (a and c) and MoS_2 (b and d). In images (b,d) the purple balls represent Molybdenum atoms while the yellow balls represent sulphur atoms.

tive[Balandin et al., 2008] material ever measured. Its electrical properties also hold great promise as it has the highest electron mobility[Bolotin et al., 2008; Du et al., 2008] ever measured in a material. At the heart of these exceptional physical properties is graphene's two dimensional nature[1], unique band structure, and crystal quality.

Graphene may be the quintessential two dimensional material but it is only a single member of a much larger family of atomically and molecularly thin two dimensional materials. Two dimensional materials have garnered much interest due to their unique properties and applications. The exceptionally thin nature is promising towards developing next generation electronic materials. Also, as every atom in the material is on the surface, they hold great potential as chemical sensors. Two dimensional materials also allow one to experimentally explore physics of electrons confined to two dimensions with relatively simple tabletop experiments. While interesting in isolation, two dimensional materials can be stacked onto each other to make custom designer three dimensional materials that cannot be found in nature.

There is a broad family of two dimensional materials that are just being explored with a wide variety of material properties. Graphene is the most studied two dimensional material with the highest Young's modulus, breaking strength[Lee et al., 2008], and thermal conductivity of any measured material. Also, as a semi-metal with its unique Dirac cone band structure, electrons in graphene travel at relativistic velocities. This invites applications in novel quantum and ballistic computing schemes as well as conventional high speed electronics.

[1]To call a material 0, 1, or 2 dimensional seems counterintuitive as all material occupies three dimensional space. The number of dimensions that electrons can propagate through a material is the simplest criteria to define low dimensional materials. Hence a quantum dot is a zero dimensional material, a nanotube is a one dimensional material, and graphene is a two dimensional material.

Beyond graphene there are other two dimensional materials such an insulating boron nitride, with a hexagonal structure like graphene but with boron and nitrogen atoms. There are also transition metal dicalcogenides (TMDCs) such as MoS_2 and WSe_2 that are generally semiconducting with band gaps ranging from 1 to 2.5 eV.

I.2 Two Dimensional Materials as Hard and Soft Materials

Graphene and other pristine two dimensional materials have a unique property in that they can be strained to near their breaking point and then relax back to their prestrained state without any undergoing any plastic deformation[Lee et al., 2008; Bertolazzi et al., 2011]. This unusual property is due to the exceptional crystal quality of these materials. In conventional bulk materials the ultimate yield strength is due to defects and grains in the crystal lattice that slide along each other.

The exceptional breaking strength of of two dimensional materials and how they undergo elastic deformation for over 10% strain is an example of how two dimensional materials behave as a classic hard material. However, to understand these materials one must also look at their soft aspects. This soft behaviour is also manifest in graphene's Young's modulus. Graphene has an in-plane stiffness (the two dimensional analog to Young's modulus) of 340 Nm^{-1}[Lee et al., 2008] and is due to the spring constant of the molecular potentials. However, at very low strains, graphene has a much lower in-plane stiffness. This lower in-plane strain is due to out of plane ripples, or flexural phonons, that can dominate graphene's material properties. These out of plane ripples significantly lower graphene's in-plane stiffness as they cause graphene to behave as an entropic spring at low strains. This entropic in-plane stiffness is explored in chapter V.

Another area where graphene's soft behavior manifests itself is its negative coefficient of thermal expansion. In a standard hard material thermal expansion is determined by the anharmonic nature of the molecular potentials. As more energy is put into these potentials the inter-atomic spacing increases and the material expands. However, graphene and other two dimensional materials behave as soft materials. This softness is manifest in the flexural phonons. As the material is heated, energy is put into the flexural phonons and the overall material ripples and shrinks, see figure I.3, leading graphene to have a negative coefficient of thermal expansion. This negative thermal expansion is explored in chapter III and has been also demonstrated by several groups[Chen et al., 2009; Singh et al., 2010].

I.3 Strain

By controllably straining a material, it is possible to study its mechanical properties. Strain is defined as

$$\varepsilon = \frac{\Delta L}{L} \tag{I.1}$$

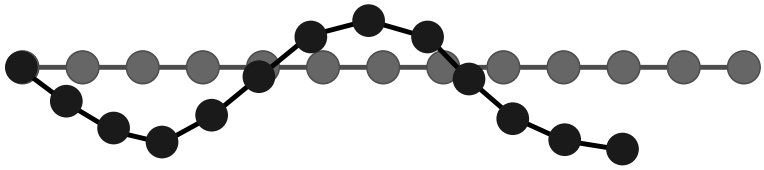

Figure I.3: Schematic of negative thermal expansion on two dimensional materials. Increased energy in the system drives increases the magnitude of out of plane fluxuations, flexual phonons, in the material, causes the material to shrink in the lateral dimension as it is heated.

where ΔL is the change of length of a material and L is the length of the material. Strain not only changes the material's size and internal forces, but can also be used to probe and control the thermal and electronic properties of materials. The most famous case of this is in strained silicon, used in all modern processors. Silicon is strained in processors in order to lower the effective mass of the charge carriers yielding higher mobility silicon transistors, crucial to the gigahertz speed computers that are used in modern microprocessors[Luo and Nayak, 2007]. Beyond controlling effective masses, strain is also used to tune the band structure of a variety of materials. It can even be used to change the optical nature of a material and has been shown to change indirect germanium into a direct band gap material[Sánchez-Pérez et al., 2011].

Materials are strained through the application of a pressure. The relation between strain and a pressure can be most simply expressed as $P = \varepsilon E$ where P is the applied pressure and E is the Young's Modulus. This standard expression falls short for two dimensional materials due to the poorly defined thickness of a two dimensional material. This is readily apparent in graphene, consisting of a single atomic layer of carbon atoms. If the material is one atom thick, how thick is the material? Is it the Bohr radius of a carbon atom (a fuzzy quantum mechanical quantity of the average distance of electrons from the nucleus), the thickness that one measures with the atomic force microscope (that includes graphene/substrate and graphene/tip interactions), or the spacing between graphite layers (which is really a measure of the balance of van der Waals forces and Pauli exclusion?) Instead of attempting to define absolute lengths on a quantum mechanical system, it is more useful to consider the in-plane stiffness M, instead of the traditional Young's modulus. This changes the expression to

$$\frac{F}{l} = \varepsilon M, \tag{I.2}$$

where F is the force exerted on the material, l is the length of material that the force is exerted on the material.

Two dimensional materials, such as Graphene and MoS_2, are particularly interesting to probe through strain due to the interplay of their hard and soft characteristics. In chapter IV, I demonstrate several of the hard material properties that can be modified through strain. Namely, the band gap is strain tunable and the material can be transitioned from a direct band gap material to an indirect band gap material.

I.4 Strain Dependence of Flexural Phonons

Crystals are often drawn as ball and stick models as shown in figure I.2. These simplistic snapshots of a crystal ignore that they atoms are in constant motion, wiggles and moving with respect to each other. These motions can be decoupled into plane waves and are called phonons. Phonons are crucial to understanding the thermal, mechanical and electrical properties of a material. There is a peculiar phonon mode that is unique to two dimensional materials, flexural phonons. These flexual phonons are due to the ability of graphene to ripple out of plane, see figure I.4.

The dispersion relation of these phonons demonstrates the unique role that they play in two dimensional materials. Figure I.5, adapted from reference [Mounet and Marzari, 2005], shows the phonon dispersion relation of graphene, with the flexural phonons labeled ZA. This phonon mode is quadratic rather than linear like the other acoustic phonon modes. The dispersion relation of this mode can be expressed as[de Andres et al., 2012]

$$\omega_q = \sqrt{\frac{\kappa |q|^4}{\rho}} \tag{I.3}$$

where ω_q is the frequency of the phonon mode, κ is the bending modulus, q is the momentum of the phonon mode, and ρ is the mass density of the graphene crystal. This can be rewritten as number of modes at a given frequency,

$$N(\omega) = \frac{1}{4\pi\sqrt{\kappa}} \frac{1}{e^{\frac{\hbar\omega}{kT}} - 1} \tag{I.4}$$

where k is Boltzmann's constant and T is the temperature. What makes this equation noteworthy is that the number of modes diverges at finite temperatures for low frequency phonons.

The situation is dramatically different in the presence of tensile strain. The dispersion relation is now

$$\omega_q = \sqrt{\frac{\kappa |q|^4 + 2(\lambda + \mu)\varepsilon |q|^2}{\rho}} \tag{I.5}$$

where λ and μ are the Lamé coefficients[2] and ε is the strain. As strain increases, the dispersion relation changes from quadratic to linear and the number of modes decreases dramatically. This leads to the interesting situation where flexural phonons are expected to dominate a material's properties at low strains but become a much more modest contribution in strained samples.

The divergent number of flexual phonons sheds light on another area where graphene has attracted a wide range of interest. A diverse number of thermal conductivities, ranging from $5 \times 10^3 W m^{-1} K^{-1}$ [Balandin et al., 2008; Lee et al., 2011] and low as $100\ W m^{-1} K^{-1}$[Jang et al., 2013], have been measured in graphene.

[2]Lamé coefficients are an alternative way than Young's modulus to map stress strain relationships. The basis is that one can write stress strain as $\sigma = 2\mu\varepsilon + \lambda tr(\varepsilon) I$

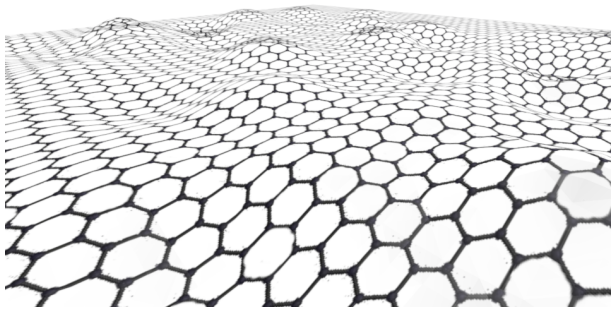

Figure I.4: Flexural phonons in graphene: as a two dimensional material, graphene can ripple out of plane. These out of plane ripples are known as flexual phonons and can dominate graphene's mechanical, thermal, and electrical properties.

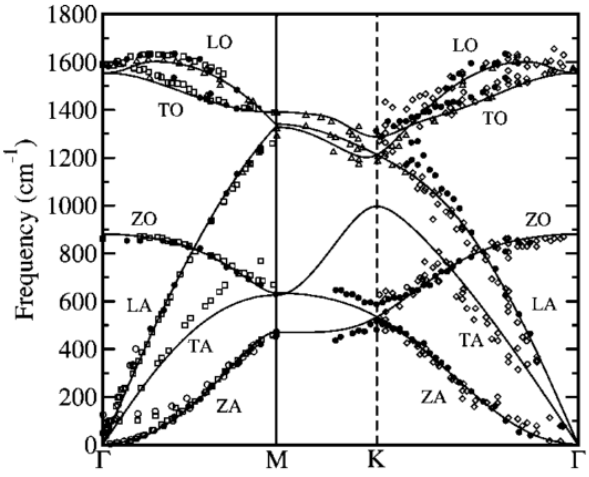

Figure I.5: Dispersion relation of unstrained graphene sheet, adapted from ref. [Mounet and Marzari, 2005]

Thermal conductivity is an important figure of merit of a material, as materials with large thermal conductivities are of particular interest for heat sink applications for the semiconductor industry. A possible way to understand the disparity of reported thermal conductivities is that flexual phonons may be the principle heat transport mechanism in graphene[Lindsay et al., 2010]. While any given flexural phonon is not effective at heat transport, the divergent number of these phonons gives these phonons an outsized role. However, as these flexural phonons are very sensitive to strain, the large range of reported thermal conductivities may be due to the uncontrolled and different strain from each study, as well as the diversity of substrates used in these studies.

I.5 Outline of Dissertation

This thesis is divided into several sections. Chapter II focuses on measuring and controlling strain in two-dimensional materials. In Chapter III, graphene's thermal expansion is probed using bimetallic cantilevers. This chapter discuses how thermal expansion and even adhesion of two dimensional films is dependent of flexual phonons. Chapter IV then focuses on one particular method of strain engineering, beam bending, and demonstrates how strain engineering can be used to tune the band structure of MoS_2. Chapter V covers how entropy and the soft nature of graphene are crucial to understanding the mechanics of graphene. Graphene is shown to be an 2D entropic membrane, many times softer than assumed in the literature. Finally, Chapter VI proposes several new avenues that are opened up by this research.

CHAPTER II

Measuring and Engineering Strain in Two-Dimensional Materials

II.1 Introduction

A key technical aspect of this dissertation is physically stretching or bending a two dimensional material. While strain is an exciting method to probe and control nanoscale materials, it is non-trivial to determine and engineer strained nanoscale devices. Raman spectroscopy, beam bending and direct imaging are introduced as methods to measure strain in two-dimensional materials. Also, methods to apply strain to materials are explored, with their various strengths and weaknesses.

II.2 Raman Spectroscopy

The traditional tool to probe strain in thin films[Wolf, 1996] and nanomaterials[Shiri et al., 2008; Sánchez-Pérez et al., 2011] is Raman spectroscopy. Raman spectroscopy probes the vibrational modes of a crystal. This is done by illuminating a sample with light. This light inelastically scatters on a material, shifting the energy of the photon by the energy of the vibrational mode of of which it scatters. As Raman spectroscopy probes the molecular vibrational modes of a material, this enables one to directly measure strain via Raman spectrascopy due to the anharmonic nature of molecular potentials.

Raman spectra is also dependent on the polarization of the incoming light. There are two unit vectors that can be used to describe phonons in a two dimensional material. These leads to two degenerate vibrational modes. These two phonons interact with polarized light that is parallel with the phonon mode. Due to this, it is common for a commercial Raman system to use circularly polarized light in order to equally capture information due to both linear polarizations. However, under uniaxial strain, the degeneracy between these two phonon modes is lifted and two Raman peaks become apparent. Probing these peaks with linearly polarized light enables one to measure the angle between the crystal latice and applied uniaxial strain. This same mechanism can also be used to determine if the sample is uniformly strained as Raman modes will still shift, but the degeneracy of these two modes will not be lifted.

Despite the power of Raman spectroscopy at determining strain, it is challenging to carry out in a cryostat or vacuum chamber, limiting is applicability. Also, Raman spectroscopy is not sensitive to small strains or changes of strain less than 0.1%.

Raman spectroscopy is also completely insensitive to strain when a two dimensional material behaves as a soft material. At low strain, two dimensional materials are dominated by out of plane ripples. As the material is strained and these out of plane ripples are pulled out, a material can undergo a considerable change in size

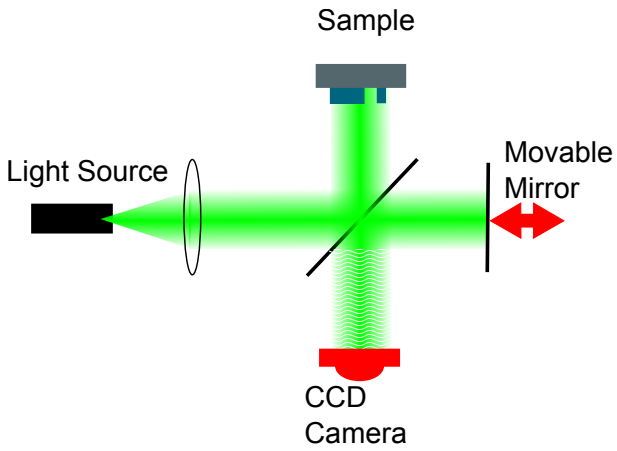

Figure II.1: **Phase Interference Microscopy** Phase interference microscopy works by illuminating a sample with monochromatic light and interfering that light with a reference beam that has a movable mirror. By moving the mirror the interference fringes on the sample shift. By analyzing the position and movement of these fringes one can extract the topography of the sample.

with negligible change in interatomic distances. Hence, if one were to use Raman spectroscopy to probe the stiffness of graphene, one would measure the inter-atomic in-plane stiffness and completely miss the entropic part.

II.3 Interferometric Profilometry

One approach to probing strain is to directly measure how the material changes in size. This has been traditionally done using either scanning electron microscopes (SEM) or atomic force microscopes (AFM). Both of these imaging techniques have significant limitations. An SEM must operate in vacuum and it cannot accurately probe changes in topography. An AFM is perhaps the best tool to explore the topography of a sample, but physically pushes on the sample, significantly perturbing soft samples like two dimensional materials.

However we can also probe samples optically using iterferometric profilometry. When employed in the phase shift mode, this form of microscopy is illustrated in figure II.1. The basic principle of operation of this profilometer is to interfere light reflecting from the sample with light from a reference beam. This creates an image that contains interference fringes. To extract height data from this, one then either moves the sample (vertical scanning interferometry or VSI) or the reference mirror (phase scanning profilometer or PSI) and images the interference fringes as they move.

This mode of profilometry enables one to extract sub-nanometer resolution height data from a sample of interest in a rapid non-destructive manner. It can take several seconds to collect the same data that would take tens of minutes with an atomic force microscope. It can also image ultra soft materials without deforming

them. These useful features come at a price. Despite the sub-nanometer vertical resolution, lateral resolution is limited $\sim$ 500 nm. Different materials will reflect light with different phase offsets, causing inconsistent height data from dissimilar materials. Also, in the PSI mode one cannot measure distances greater than $\sim$ 500 nm. Finally, when imaging transparent substrates, such as silicon oxide or graphene, the instrument can cannot always distinguish interference patterns from the upper part of the sample and the underlying parts of the sample.

II.4 Graphene Mechanical Resonators

An alternate route to determine the strain of a two dimensional material is through mechanical resonance. Conceptually, this is easy to visualize with a guitar string. The frequency of the note that is played on a guitar string depends on the tension on the string. Tuning a guitar consists of straining the string until the resonant frequency of the string matches some desired frequency. The inverse is also possible, by listening to the guitar string, one can know how much strain the string is under. This exact same principle applies to a nanoscale graphene sheet as it does to a guitar. Following the work by Changyao Chen[Chen, 2013] a model of graphene mechanical resonators as one dimensional strings is presented in the following sections.

II.4.1 Continuum Mechanics Model of Graphene Resonator

A graphene device, such as the one in figure II.3 has been shown to behave like a one dimensional spring under tension[Bunch et al., 2007; Chen et al., 2009; Singh et al., 2010; Zande et al., 2010]. The resonant frequency of a string under tension is

$$f = \frac{n}{2L}\sqrt{\frac{T}{\mu}} \tag{II.1}$$

where n is the mode number, L is the length, T is the tension on the sheet, and μ is the mass. For a two dimensional material like graphene tension is

$$T = M\varepsilon \tag{II.2}$$

where M is the in-plane stiffness of graphene, which is typically assumed to be 340 N/m, but in chapter V we show that this may not always be the case ., and ε is the strain of the device. The mass density of the sheet consists of more than just the mass of the graphene, but also includes the accumulated residue from fabrication. This accumulation is often multiple times more than the mass of the graphene itself. Hence mass is generally expressed as

$$\mu = a\rho_0 \tag{II.3}$$

where ρ_0 is the mass area density of graphene and a accounts for the amount of gunk on the 2D material, expressed in multiples of the mass density of graphene. Putting these together leads to

$$f = \frac{n}{2L}\sqrt{\frac{M\varepsilon}{a\rho_0}}. \tag{II.4}$$

On the surface, this is not a useful method to extract the strain of a two dimensional material as one cannot decouple strain from the mass. However, the next section shows how this can be overcome by controlling tension in graphene via electrostatic pulling with an applied gate voltage.

II.4.2 Spring Constant Softening

An interesting aspect of graphene is that its resonant frequency is gate dependent. In order to understand how the spring constant of graphene or another two dimensional material depends on gate voltage, first it is useful to derive the strain (or tension) a graphene sheet undergoes with an applied gate voltage. In the graphene sheet of length L, strain is

$$\varepsilon = \frac{\int_0^L \sqrt{1+\frac{dy^2}{dx^2}}dx - L}{L} \tag{II.5}$$

$$\varepsilon = \frac{\int_0^L \sqrt{1+(\frac{\xi(x)}{dx})^2}dx - L}{L} \tag{II.6}$$

$$\varepsilon \approx \frac{L - \int_0^L \frac{1}{2}\xi'^2 dx - L}{L} = \int_0^L \frac{1}{2L}\xi'^2 dx \tag{II.7}$$

Assuming that graphene has zero bending stiffness and $\xi(x)_{max} << L$ then the line shape is[Weaver et al., 1990]

$$\xi(x) = z\frac{4}{L^2}(Lx - x^2). \tag{II.8}$$

strain can then be simplified to

$$\varepsilon = \frac{8z^2}{3L^2} \tag{II.9}$$

This yields a simple expression for strain of a graphene resonator under a uniform force, such as an electric field.

In order to calculate the deflection of a clamped graphene sheet in the presence of an electric field we assume that the elastic energy stored in the strained resonator is

$$U_{el}(\xi(x)) = \int_0^L \frac{L}{2}\xi'^2 dx = \int_0^L \xi'^2(x)(\frac{T_0}{2} + \frac{Mw}{4L}\int_0^L \xi'^2(u)du)dx \tag{II.10}$$

where ξ is the mode shape of the stretched string, L is the length of the resonator, M and L are the in-plane

stiffness and the width of the device. Inserting equation II.8 into equation II.10 yields

$$U_{el} = \frac{8ES\varepsilon_0 z^2}{3L} + \frac{64Mwz^4}{9L^3} \tag{II.11}$$

To account the electrostatic force between the graphene and the gate we treat this system as a parallel plate capacitor, yielding an electrostatic energy of

$$U_{es} = -\frac{1}{2}C_g V_g^2 \tag{II.12}$$

As this is a mechanical object, it is important to remember that capacitance is not a constant value but will change depending on the distance of the resonator from the gate, accordingly we expand $C_g \approx C_0 + C'z + C''z^2/2$, where $C' = dC_g/dz$, $C'' = d^2C_g/dz^2$.

Now the equation of motion can be simplified to

$$\frac{dU}{dx} = \frac{256Mw}{9L^3}z^3 + \frac{16Mw\varepsilon_0}{3L}z - \frac{1}{2}C''V_g^2 z - \frac{1}{2}C'V_g^2 = 0 \tag{II.13}$$

Putting the equation in the form $\alpha z^3 + \beta z^2 + \gamma$ we can solve for z at equilibrium, yielding

$$z_e = -\frac{0.87\beta}{\sqrt[3]{9\alpha^2\gamma + 1.7\sqrt{4\alpha^3\beta^3 + 27\alpha^4\gamma^2}}} + \frac{\sqrt[3]{9\alpha^2\gamma + 1.7\sqrt{4\alpha^3\beta^3 + 27\alpha^4\gamma^2}}}{2.6\alpha} \tag{II.14}$$

where

$$\alpha = \frac{256Mw}{9L^3} \tag{II.15}$$

$$\beta = \frac{16Mw\varepsilon_0}{3L} - \frac{1}{2}C''V_{gate}^2 \tag{II.16}$$

$$\gamma = -\frac{1}{2}C'V_{gate}^2 \tag{II.17}$$

With a proper framework for the strain that a graphene sheet will be subjected to, we model the resonant frequency of a one dimensional string as

$$f = \frac{1}{2\pi}\sqrt{\frac{k}{m_{eff}}} \tag{II.18}$$

where k is the spring constant of the material and m_{eff} is the effective mass of the mechanical resonator. Now, by applying an electrostatic force with the gate on the graphene we can change the spring constant and independently fit both the mass and $M\varepsilon$.

The spring constant k is

$$\frac{\partial^2(U_e l + U_e s)}{\partial z^2}|_{z_e} = \frac{6ES\varepsilon_0}{3L} + \frac{256ES}{3L^3}z_e^2 - \frac{1}{2}C''V_g^2 \tag{II.19}$$

Equations II.18 and II.19 yield the resonant frequency of a graphene resonator over a wide range of gate voltages and enables one to fit the equation to find $M\varepsilon$ and mass on the device. While this appears to be an excellent method to extract the built-in strain of a sample, it requires a detailed knowledge of the in-plane stiffness, a quantity that is dependent on both strain and temperature as shown in chapter V.

II.4.3 Measuring Graphene Mechanical Resonators

Mechanical resonances in suspended graphene devices can be directly measured using an all electrical measurement setup[Chen, 2013; Xu et al., 2010]. Using devices like the one in figure II.3, the mechanical resonance can be electrically detected by applying a modulated voltage V_{gate} to the gate.

The current that one measures in this type of set up is[Xu et al., 2010]

$$\tilde{I} = i\omega C_{tot}\tilde{V}_g - i\omega\frac{\tilde{z}}{z_0}C_g V_g + V_d\frac{dG}{dV_g}\tilde{V}_g - V_d\frac{dG}{dV_g}\frac{\tilde{z}}{z_0}V_g \tag{II.20}$$

where $\tilde{I}$ and $\tilde{V}$ is the modulated current and modulated voltage, ω is the frequency, V_d is the source drain bias, and G is the conductance. Of these four terms, the first and third are purely electrical while the second and fourth terms are mechanical in nature.

The first term is just the standard reactance of a capacitor. This relationship sets the highest frequency that can be measured. We can think of this circuit as a low pass filter[Sazonova, 2006] with a corner frequency of

$$f_{corner} = \frac{1}{2\pi RC} \tag{II.21}$$

where R is the resistance and C is the capacitance of the device. For most devices in the literature, this frequency is typically less than 100 kHz, requiring the use of mixing circuits or optical readout to detect the oscillators motion[Sazonova et al., 2004; Sazonova, 2006; Bunch et al., 2007; Chen et al., 2009; Zande et al., 2010]. By fabricating a local gate on an insulating substrate (undoped silicon), one can have a much smaller capacitance and a much larger corner frequency.

The next two terms in equation II.20 are small and considered insignificant in this thesis. The final term is due to mechanical motion of the oscillator and is the signal of primary interest.

In order to measure this final term we employ the circuit in figure II.2. This circuit enables us to apply a voltage to both the source and the gate while probing the high frequency characteristics of a graphene

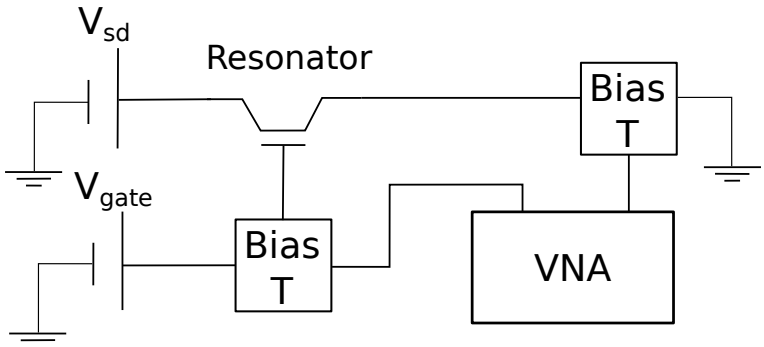

Figure II.2: Circuit employed to measure the mechanical resonance of the graphene devices. VNA is a vector network analyzer.

resonator. Typically the network analyzer is driving with a power of -35 dbm and the S_{21} parameter is analyzed.

Data collected with the network analyzer produces a large variety of line shapes. The resonant frequency and quality factor of these curves are accurately measured using a phase dependent Lorenzian with background[Sazonova, 2006].

$$I(f) = A + Bf + \frac{H\cos(\arctan(\frac{f_0^2 - f^2}{\Gamma f} + \Delta\phi))}{\sqrt{(1-(\frac{f}{f_0})^2)^2 + (\Gamma\frac{f}{f_0})^2}} \tag{II.22}$$

where A, B, H, f_0, Γ and $\Delta\phi$ are independent fitting parameters. A and B are to fit the background, H fits the height of the peak while f_0 and Γ fit the location and the width of the peak respectively. $\Delta\phi$ is the phase of the Lorentzian. An important quantity for mechanical resonators, the quality factor Q, can be found by

$$Q^{-1} = \frac{\Gamma}{f_0}. \tag{II.23}$$

II.5 Strain via electrostatic gate

A simple method to apply strain in suspended samples via an electrostatic gate on a suspended graphene sheet, such as the one in figure II.3. In these devices a voltage can be applied to the gate electrode, pulling down the sheet. The strain on a sheet of graphene, like the one in figure II.3, can be modeled by classical continuum mechanics. The pressure on the sheet is

$$\Delta P = 1/2\frac{C'}{A}V_g^2 \tag{II.24}$$

where C' is the derivative of the capacitance with respect to gate distance, A is the area of the sheet, and V_g is the voltage on the gate. The precise strain that a sheet undergoes due to this pressure is due to the precise

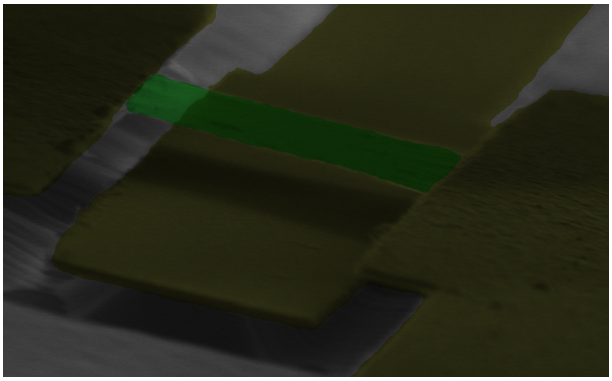

Figure II.3: **Suspended graphene device** Flase color SEM image of graphene device used to probe mechanical properities. A single sheet of graphene is suspended between two electrodes above a local gate.

geometry and in-plane stiffness.

For the geometry in figure II.3, strain is calculated by solving the height, h_0 that the membrane is deflected under a bias[Bao et al., 2012].

$$\frac{\varepsilon_0}{2}\left(\frac{\varepsilon_r}{\varepsilon_r d_1 + d_2}\right)^2 V_g^2 \times L^2 = \frac{64}{3}\frac{M}{L^2}h_0^3 \tag{II.25}$$

where ε_r is the dielectric permitivity of silicon oxide, d_1 is the distance between the graphene and oxide, d_2 is the oxide thickness, V_g is the oxide thickness, L is the length of the suspended graphene, and M is the in-plane stiffness of graphene. For a normal device with the in-plane stiffness due to inter-atomic bonds, this leads to a strain $< 0.01\%$ per volt applied to the film. This highlights the ability to probe small strains using gate bias.

A common effect in graphene that can complicate this idea is that graphene devices generally have some doping. A pristine sheet of graphene should have no doping with the Fermi level between the upper and lower band. However in typical graphene devices one experimental finds that they are doped. This doping is probably due to fabrication residue on the device and is generally manifest in the charge neutrality point of graphene being shifted from zero volts. The charge neutrality point is where there is the minimum number of charge carriers in graphene that can contribute to conductivity. The experimental manifestation of doping can be found by measuring the resistance of a device while changing the gate voltage. At the charge neutrality point, where the resistance is maximum. The gating from the device offsets the doping of the graphene.

This leads to the question of where zero force is for a graphene membrane under an electrostatic potential. Is it at zero volts or at the charge neutrality point? To clarify this, I propose a simple model for dopants in graphene. If one assumes that most of the dopants in graphene are charged particles that are in close proximity to the graphene membrane, then the charge that one electrically measures in graphene are actually induced charges due to the nearby dopants. So even though there are charges on a graphene sheet, the sheet as a whole

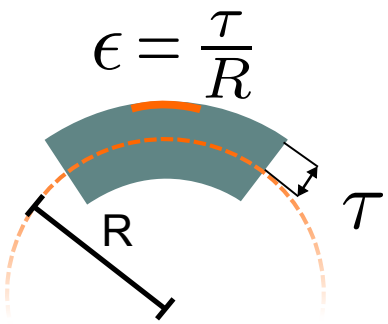

Figure II.4: **Beam Bending** Inducing strain by bending a beam. As any beam is bent the strain on the surface of the beam is $\kappa\tau$.

is charge neutral, causing zero pressure at zero volts and not at the charge neutrality point. This is born out in mechanical resonance data of graphene sheets[Bunch et al., 2007; Zande et al., 2010; Chen et al., 2009].

II.6 Four point bending

The most popular method to study strained nanomaterials is through bending the underlying substrate. This technique has been used to examine the effects due to strain in silicon, germainium, carbon nanotubes, graphene, and a host of other materials. Four point bending remains a workhorse of the experimental strain engineering community due to the ease of straining the material and the ability to probe a wide range of strains.

Assuming that the beam is bent in a circle, strain of a bent beam or substrate is $\varepsilon = \kappa\tau$, where ε is the strain, κ is the curvature of the beam or the inverse radius of curvature, and τ is the distance from the center of the beam to the region of interest. This stems from the assumption that the substrate is bent in a circle. Following figure IV.3, the length of a segment of a circle is $rd\phi$. The strain can be calculated as the change of length from the center point to the surface of the substrate and is

$$\varepsilon = \frac{\Delta L}{L} = \frac{r_1 d\phi - r_2 d\phi}{r_2 d\phi} = \frac{r_1 - r_2}{r_2} = \tau\kappa \tag{II.26}$$

where $rd\phi$ is the arc length of the beam, r_1 and r_2 are the respective radii of curvature of the surface and center point of the substrate and $d\phi$ is the angle the subtends the beam.

In order to bend the substrate, care must be taken to ensure that one can measure the radius of curvature of the beam. This is done using three or four point bending. This is done by applying pressure from one or two points under the device and two points above the device. These points of force completely determine the curvature of the bent beam enabling a researcher to know the radius of curvature from the configuration of

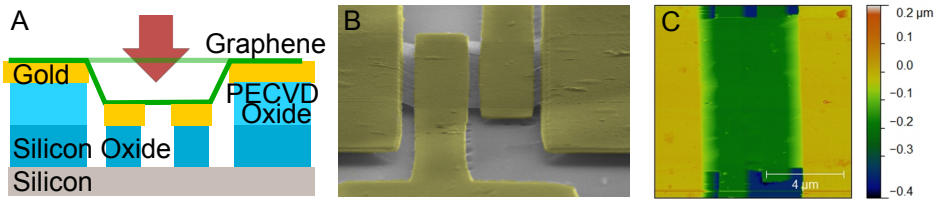

Figure II.5: **Controlled collapse** Controlled collapse of graphene devices to generate uniaxial strain. a) Schematic of a controlled collapse device. b) SEM image of a controlled collapse device. c) AFM image of a controlled collapse device.

the bending apparatus instead of having to employ a complicated scheme to measure the radius of curvature of the substrate.

Traditional bending apparatus require the material to be supported on the substrate, limiting the physics can be explored in these devices. Several complex schemes have been developed to enable suspended devices, but none that are compatible with graphene.

II.7 Controlled Collapse

An alternative method to strain engineer graphene is through patterning a substrate and causing the 2D material to collapse onto the patterned substrate. In the work by Metzger et al[Metzger et al., 2010] graphene was transferred onto patterned substrate. The graphene collapses around the resulting structure and is strained, as verified through Raman spectroscopy.

Using a similar logic I have developed a method to strain engineer suspended graphene devices through controlled collapse of graphene onto prepatterned electrodes. The efficacy of strain control was demonstrated through Raman spectroscopy.

The first step to engineering strain via this method is to have the proper prepatterned substrate. Our substrates are multilayer substrates with metal electrodes separated by silicon dioxide. Figure II.5a is a schematic of a controlled collapse substrate. Graphene is transferred onto this substrate and the substrate is etched, removing much of the silicon oxide, as seen in figure II.5a. The graphene collapses and the engineered strain is

$$\varepsilon = \frac{h^2}{La}. \tag{II.27}$$

This strain is determined by the geometry of the substrate, where h is the vertical distance between the upper and lower electrodes, L is the overall length of the graphene and a is the horizontal distance between the upper and lower electrodes. Figure II.5b and c shows SEM and AFM images of this style of device.

To verify that this is a viable method to engineer strain we measured the Raman shift of controlled

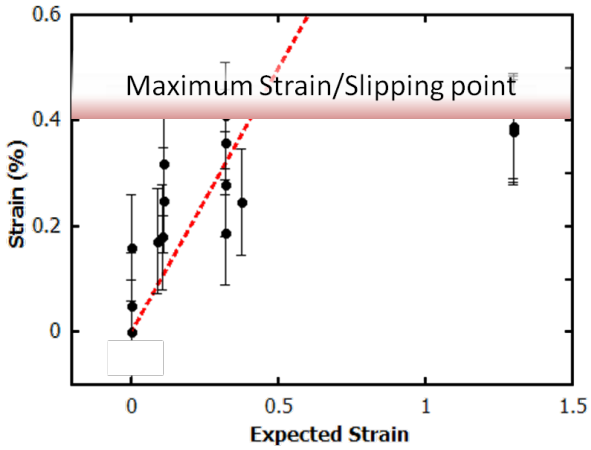

Figure II.6: **Engineered strain** Engineered strain versus actual strain for a number of controlled collapsed devices where strain is extracted from the shift in the raman peaks.

collapsed devices[Mohiuddin et al., 2009], see figure II.6. Initially, at low strains we get a large amount of noise due to the intrinsic strain of the graphene device due to the vagarities of the transfer process. The devices track the engineered strain to a point, but do not continue to be strained at higher engineered strains. The could be due to slipping or incomplete collapse.

While for the purpose of this dissertation, only geometries enabling uniform strain were explored, it is straightforward to design the underlying substrates that would allow one to explore non uniform strain in two dimensional materials.

The principle limitations of this style of strain engineering is that only tensile strain can be explored and only one magnitude of strain can be engineered in a single device. This allows one to say what happens at one strain but requires a large number of samples to extract how the material behaves under a range of strains. These devices also suffer low yield.

II.8 Thermal Expansion of Contacts

Strain can also be set through the thermal expansion of the materials supporting the graphene device. A simple graphene device, seen in figure II.3, consists of graphene and the supporting gold contacts. As the device is cooled down, thermal expansion causes the gold to shrink and graphene to expand. The strain this induces in the device is

$$\varepsilon = \int \alpha_{graphene}(T)dT + \frac{L_{gold}}{L_{graphene}} \int \alpha_{gold}(T)dT \tag{II.28}$$

where $\alpha(T)$ is the coefficient of thermal expansion of graphene or gold, and L_{gold} is the length of suspended gold.

Figure II.6 contains data of measured versus engineered strain for a range of these devices. First one must note that the measured strain is less than the engineered strain. This is due to the negative thermal expansion of graphene, enabling the fabrication of slack devices. Also the upper limit of strain shown in this figure is currently limited by our ability to measure high frequencies, and we suspect that higher strains can be obtained.

A limitation of this style of strain engineering is that strain is only induced at low temperatures, severely limiting the range of temperatures where strain dependent phenomena can be explored.

II.9 Conclusion

In conclusion, Raman microscopy, direct imaging with interferometric profilometery, and mechanical resonance enables one to determine the strain of two dimensional materials. We show a range of methods that can be utilized to engineer strain in two dimensional materials and demonstrate strain engineering from slack devices to devices with 0.3% strain.

CHAPTER III

Probing Strain and Adhesion with Bimetallic Cantilevers

III.1 Introduction

In this chapter, I probe graphene's coefficient of thermal expansion and adhesion between graphene and a substrate using bimetallic-like cantilevers. These measurements demonstrated several ways that graphene behaves as a 'soft' material. First, we measured graphene's negative coefficient of thermal expansion and specifically demonstrated how this coefficient of thermal expansion becomes smaller in magnitude when more layers of graphene are present, damping the flexual phonons that dominate thermal expansion of these materials. Second we note that adhesion of graphene to the silicon nitride substrate is temperature-dependent. We postulate that this is once again due to these flexuaral modes. As more energy is dumped into these modes the distance between graphene and the substrate increases and the Van der Waals forces that holds these two materials together dramatically decreases. This work has been previously published in Nano Letters[Conley et al., 2011].

Here, we develop a technique to probe the mechanical properties of graphene films *attached to substrates.* At the heart of this technique are suspended bimetallic-like cantilevers consisting of a well-characterized substrate layer and a layer of test material, such as graphene. By measuring the deflection of these cantilevers as a function of temperature we are able to extract graphene's in-plane isotropic strain, coefficient of thermal expansion, and estimate the frictional forces between graphene and the substrate.

To explore the interaction of graphene with a range of substrates, we studied cantilevers with either a silicon nitride (SiN_x) or gold (Au) substrates and either single (1xGr), double (2xGr), or triple (3xGr) layer graphene films attached to the substrate. We fabricated and measured four 1xGr/SiN_x devices, one 2xGr/SiN_x device, two 3xGr/SiN_x devices, and nine 1xGr/Au devices (Figs. III.1a,b).

III.2 Fabrication

Overview of graphene growth and transfer of graphene onto the determined substrate is covered in this section followed by fabrication details of both the silicon nitride and gold cantilevers fabricated for this study, see figure III.1. The principle advantage of the graphene silicon nitride cantilevers is that they were much larger than the graphene gold cantilevers and were much more robust, allowing for less noisy data collection.

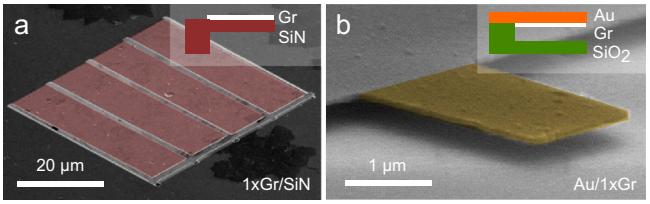

Figure III.1: **SEM images of the graphene bimetallic-like cantilevers following fabrication.** a) Single layer graphene/silicon nitride (1xGr/SiN_x) cantilever, the suspended part false-colored red. b) Gold/Single layer graphene (Au/1xGr) cantilever, the suspended part false-colored yellow. Insets: Cartoon views of the devices.

III.2.1 Graphene Growth and Transfer

In order to make graphene bimetallic cantilevers one needs graphene. Graphene for this study was grown following recipes developed previously[Li et al., 2009]. Growth is done in a custom 1" vacuum CVD furnace. Our growth recipe is as follows. After cleaning the copper foils in acedic acid overnight the copper foils are blown dry and loaded into the CVD furnace. The foils are heated up to 1000 C with 10 sccm of H_2 and annealed at 1000 C for ≈20 minutes. 10 sccm of methane of flowed in the furnace with the hydrogen for 20 minutes and the copper is then quickly pulled out of the furnace. The sample is cooled in the methane hydrogen environment.

These Graphene/Cu foils were cut into 1cm x 1cm squares. In order to transfer graphene onto a SiN_x membrane, we first spun PMMA 950K A11 resist support layer onto Graphene/Cu foils at 2000 rpm for 45 secs. PMMA was then baked at 180° C; Nitto Denko Revalpha thermal release tape (Semicorp.com, item No. 3198) was used to assist in the spinning process to avoid physical damage to the foil. The PMMA/-Graphene/Cu foil was then placed in Cu Etchant Type CE100 (Transene Company) for >5 hours to etch away the bottom Cu layer. After the etching was completed, the PMMA/Graphene film was rinsed in deionized water bath for 30 min, and then transferred onto the silicon nitride membranes. The transfer fidelity was improved by placing a drop of PMMA dissolved in anisole onto the PMMA/graphene film and baking it on a hot plate at 45° C for 1 hour. Finally, to remove the PMMA resist, the sample was placed in an acetone bath for 12 hours, rinsed in isopropanol for 30s and dried with dry nitrogen gas. It is important to note that the much larger thermal expansion coefficient of liquid compared to solid PMMA may generate a significant strain in graphene, *even before it is deposited onto a target substrate*

III.2.2 Gold Graphene Cantilevers

The fabrication procedure of 1xGr/Au cantilevers is done by transferring a single layer of CVD-grown graphene onto a SiO_2 (300nm)/Si substrate. We pattern the graphene via a combination of electron-beam

lithography and oxygen-plasma etching and then thermally evaporate a 50 nm thick layer of gold on top of the device. Cantilevers are released by etching 200 nm of the oxide in hydrofluoric acid[Bolotin et al., 2008]. The fabricated cantilevers are 2-3 μm wide and 2-4 μm long and are suspended 200 nm above the SiO_2 substrate.

III.2.3 Silicon Nitride Graphene Cantilevers

To fabricate 1xGr/SiN_x (2xGr/SiN_x or 3xGr/SiN_x) devices we successively transfer the target number of single layer graphene sheets grown by chemical vapor deposition (CVD) on copper foils [Li et al., 2009] onto a suspended 188 nm thick, low-stress silicon nitride membrane supported by a silicon frame. Individual cantilevers are cut out of the membrane using a focused Ga ion beam. The fabrication procedure yields suspended cantilevers that are 5-8 μm wide and 30-40 μm long.

Silicon rich silicon nitride (SiN_x) was grown on 100 mm Si wafers using low pressure chemical vapor deposition (LPCVD) furnace (Tystar Inc). Control of stress in the films was achieved through adjustment of silane/ammonia ratio following well established protocols and recipes[Habermehl, 1998; Patil et al., 2005; Temple-Boyer et al., 1998]. SiN_x films with intrinsic tensile stress of approximately 90 MPa grown at 852 C and 220 mTorr were used for cantilever fabrication in this work. The flow rates of ammonia and dichlorosilane were, respectively, 25 and 100 sccm during the LPCVD growth. Intrinsic stress in the SiN_x films on the Si substrates was measured using an FSM128 stress measurement tool (Frontier Semiconductor, Inc.) which determines stress in thin films based on the optically measured wafer curvature. For the purpose of measuring film stress, SiN_x layers were deposited on 100 mm single side polished (SSP) wafers and SiN_x was subsequently etched away from the back side using timed RIE in SF_6 plasma.

Fabrication of SiN_x membranes started with deposition of LPCVD SiN_x on 100 mm double side polished (DSP) Si (100) wafers with thicknesses in the 500 to 525 μm range. This step was followed by photolithographic patterning of square etch holes on the back side of the wafers. Positive photoresist SPR 220 4.5 (Microchem, Inc.) spun at 3000 rpm was used for this purpose. After etching SiN_x within unmasked areas using SF6 plasma RIE, and stripping remaining photoresist in hot NMP wafers were etched using 30 % aqueous KOH etch at 80 C for 7-8 hours until membranes were formed (i.e. when visual inspection of the wafers indicated formation of transparent SiN_x membranes). Wafers were then transferred into a bath with DI water and rinsed thoroughly while replacing DI water several times. Finally, wafers with SiN_x membranes were blow dried using filtered nitrogen flow.

The SiN_x layer on individual chips selected for further experiments were thinned using timed RIE etch in SF_6 plasma. Spectroscopic ellipsometry (HORIBA Jobin Yvon MM-16 tool) was used to measure thickness and refractive index of the SiN_x films. As a result of this fabrication step, we obtained suspended SiN_x

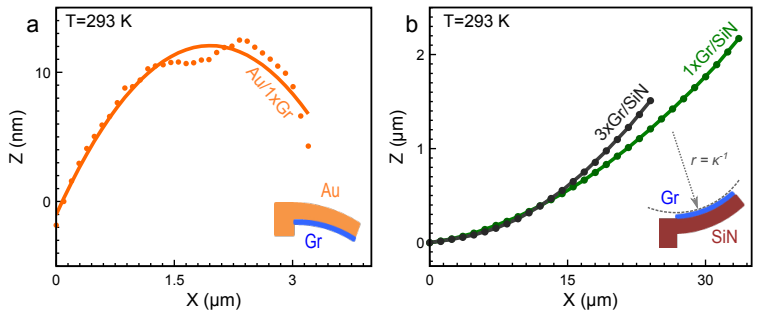

Figure III.2: **Bending of Au and SiN$_x$ substrates.** a) Representative profile $Z(X)$ of a Au/1xGr cantilever at room temperature immediately following fabrication, as obtained from interferometric profilometry. Dots are datapoints, solid line is a constant-curvature fit. Au cantilevers have a kink at the base which may be due to inelastic deformation during fabrication. b) Same, for 1xGr/SiN$_x$ and 3xGr/SiN$_x$ cantilevers. While the 1xGr/SiN$_x$ and the 3xGr/SiN$_x$ cantilevers are the same length, differences in the sample tilt prevented us from measuring the very ends of the cantilevers for the 3xGr/SiN$_x$ devices causing the apparent difference in length.

membranes 40 μm $\times$ 40 μm in area and 188nm in thickness.

III.2.4 Devices

To fabricated suspended graphene/SiN$_x$ cantilevers, we patterned the SiN$_x$ membranes using a focused Ga ion beam (FEI Nova 500 dual beam tool). We formed 3 to 4 cantilevers out of each SiN$_x$ membrane. Optical interferometric profilometry (WYKO 9800 series tool) was used to ensure that the cantilevers are intact after processing.

III.3 Strain

We analyze the mechanical properties of graphene by examining the height profiles (Z) along the length direction (X) of the bimetallic-like cantilevers from 100 K to 450 K in a nitrogen atmosphere. Interferometric profilometry (Wyko 9800, Veeco) is employed to obtain $Z(X)$ profiles with a vertical resolution of 0.1 nm (Fig. III.3, Inset). We observe three distinct trends in every device measured. First, immediately after fabrication, and at room temperature T_0=293 K, every cantilever is significantly bent (Fig. III.2). Second, after an initial annealing step, the magnitude of bending is temperature-dependent (Fig. 3). Third, in Gr/SiN$_x$ cantilevers there are changes in the bending that are irreversible during the initial heating/cooling process but become reversible in successive temperature cycling (Fig. 3c,d). We now quantitatively examine these trends and associate the first trend with the presence of significant built-in strain in graphene, the second with graphene's thermal expansion, and the third with slipping between graphene and the substrate at large strains.

We begin with the observation that immediately following fabrication every cantilever is not flat but is bent towards the graphene layer (Figs. III.3a,b). We associate this bending with the strain mismatch between

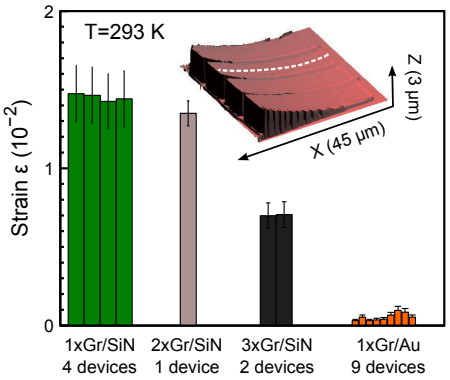

Figure III.3: **Initial strain of graphene on Au and SiN$_x$ substrates.** The strain in graphene on different substrates extracted from curvature via equation III.1. Inset: A height map of 1xGr/SiN$_x$ cantilevers obtained via interferometric profilometry. The dashed line corresponds to the $Z(X)$ profile shown in figure III.2b

graphene (ε_g) and the substrate (ε_s). A cantilever composed of unequally strained graphene and substrate layers is expected to minimize its energy by bending into an arc with a curvature κ (the inverse of radius of curvature, Fig. 2b, inset) that is proportional to $\Delta\varepsilon = \varepsilon_g - \varepsilon_s$. The analytical solution is

$$\kappa = 6\frac{E_g t_g(1-\nu_s)}{E_s t_s^2(1-\nu_g)}\Delta\varepsilon \tag{III.1}$$

where E_g,t_g,ν_g (E_s,t_s,ν_s) are the Young's modulus, the thickness, and the Poisson ratio of the graphene (substrate) layer respectively[Townsend et al., 1987]. The observed profiles Z(X) of all the cantilevers are indeed arcs with constant curvature κ (Fig. 2a,b) and so the strain level of graphene ε_g can be determined as long as the material parameters of equation III.1 are known.

Although equation (III.1) is derived for macroscopic materials, recent work on suspended graphene films suggests that such models are applicable to two-dimensional graphene assuming $E_g = 1 \pm 0.1$ TPa, $t_g = 0.35$ nm (t_g=1.05 nm for three-layer graphene), and $\nu_g = 0.165$[Bunch et al., 2007; Blakslee et al., 1970]. In a separate measurement, we determine the material parameters of our substrate materials to be $E_s = 220 \pm 13$ GPa, $t_s = 188 \pm 2$nm, $\nu_s = 0.22$ for SiN$_x$ and $E_s = 25 - 45$ GPa, $t_s = 50 \pm 2$ nm, $\nu_s = 0.44$ for gold. We also measure the built in strain ε_s in as-deposited Au and SiN$_x$ to be small ($\varepsilon_s < 4 \times 10^{-4}$) compared to ε_g, such that $\Delta\varepsilon \sim \varepsilon_g$.

Using equation III.1 to obtain ε_g from multiple datasets similar to Fig. 2a and b, we find that the graphene layer in all measured cantilevers is under significant tensile strain that is significantly larger in 1xGr/SiN$_x$ devices, $\varepsilon_g \sim 1.5 \times 10^{-2}$, compared to Au/1xGr devices, $\varepsilon_g = 1 \times 10^{-3} - 4 \times 10^{-4}$ (Fig. III.3). This difference is surprising, as we employ the same graphene growth and transfer technique, and would hence expect to find

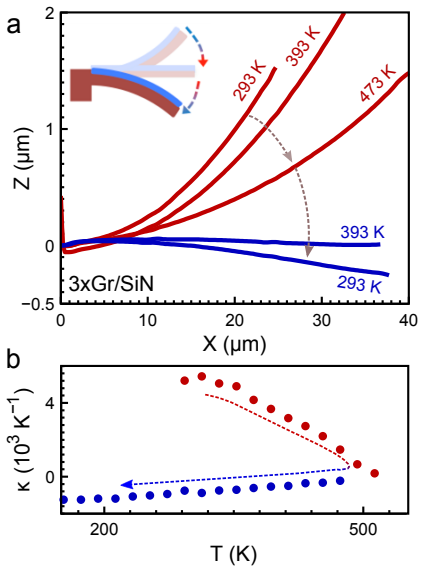

Figure III.4: **Hysteretic temperature dependence of curvature for graphene bimetallic-like cantilevers.** a) Temperature dependence of the profile $Z(x)$ of a 3xGr/SiN cantilever during the initial heating (red)/cooling (blue) cycle immediately after fabrication; the curvature κ extracted from the profile is shown in (a). Note the hysteretic behavior: κ at room temperature is reduced after heating and cooling.

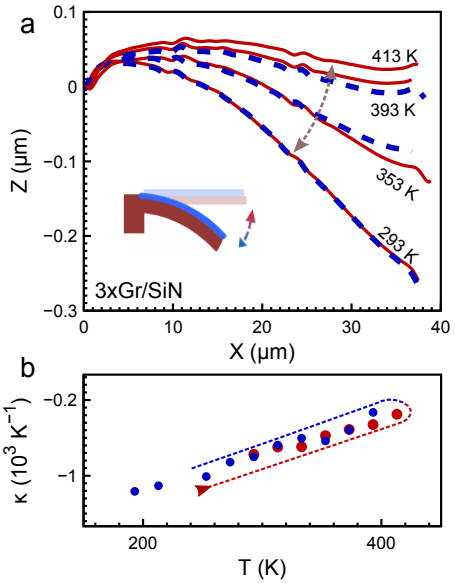

Figure III.5: **Non hysteretic temperature dependence of curvature for graphene bimetallic-like cantilevers.** The T-dependence of the profile for the same device in subsequent heating/cooling cycles; the the corresponding curvature is shown in (d). The curvature data obtained during the heating cycle are artificially offset by 10 K to emphasize the non-hysteretic behavior of $\kappa(T)$.

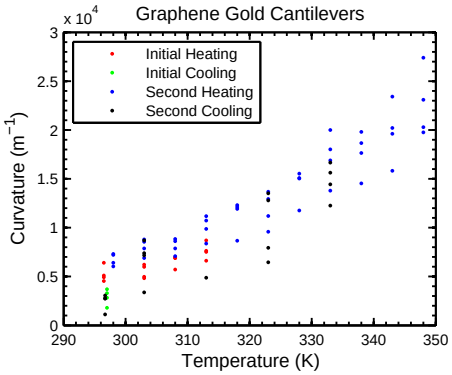

Figure III.6: Curvature versus temperature for four Au/1xGr cantilevers. The devices behave non-hysteretically from 293 C to 348 C.

graphene equally strained in both Gr/SiN_x and Au/Gr devices. In the last part of the paper we address this observation in detail, and attribute it to graphene being able to relieve part of its strain by slipping across the substrate.

III.4 Thermal Expansion

Next, we discuss a pronounced temperature dependence in the curvature of the cantilevers (Fig. 3c,d) that is extracted from their $Z(X)$ profiles (Fig. 3a,b). Initially, for the Gr/SiN_x devices, this dependence is hysteretic: the curvature of the cantilevers at room temperature changes significantly when they are first heated to T>473K and does not return to its original value when cooled back to 293K (Fig. 3c). However, this hysteretic behavior disappears after the first heating and cooling cycle and we observe that the cantilevers bend up and down reproducibly as they are heated and cooled multiple times between T=450K and 110K, without exhibiting any memory of their previous state (Fig. 3b,d).

Most of the measurements in the manuscript are based on probing the curvature of the cantilevers with respect to temperature using interferometric profilometry. An objective with magnification of 5x was used for Gr/SiN cantilevers, while higher magnification (50x) objective was necessary for smaller Gr/Au cantilevers. Importantly, the higher magnification objective was not compatible with the highest and the lowest measurement temperatures. As a result, Gr/Au cantilevers were measured at a smaller set of temperatures (293 – 348 K) compared to that of Gr/SiN_x cantilevers (100 K – 550 K). The curvature versus temperature for the gold/graphene cantilevers was observed to be non-hysteretic as can be seen in Fig. III.6.

We first focus on the non-hysteretic temperature behavior (Fig. 3d) which we ascribe to the mismatch of the coefficients of thermal expansion between graphene, $\alpha_g(T)$, and the substrate, $\alpha_s(T)$. As all materials tend to change their size with temperature as a result of thermal expansion, the strain difference between

graphene and the substrate $\Delta\varepsilon$ is also temperature dependent:

$$\Delta\varepsilon(T) = \int_{T_0}^{T} [\alpha_g(T) - \alpha_s(T)]\, dT + \Delta\varepsilon_0, \tag{III.2}$$

where $\Delta\varepsilon_0$ is the previously discussed difference in built-in strains between graphene and the substrate layers at room temperature. Thus, according to equation (III.1), we expect that the curvature κ of the cantilevers should indeed also be temperature dependent and that its temperature derivative $d\kappa/dT$ should be proportional to $\alpha_g(T) - \alpha_s(T)$. Assuming previously reported values for α_s[Martyniuk et al., 2006; Paszkowicz et al., 2004; Nix and MacNair, 1941], we now extract the coefficient of thermal expansion of graphene using equations (III.1) and (III.2).

Figure 4a shows $\alpha_g(T)$ of single layer and multilayer graphene on silicon nitride obtained from four 1xGr/SiN_x (blue curves) and two 3xGr/SiN_x (red curves) devices. The shaded regions represent uncertainty in α_g that result from uncertainties in the Young's modulus and thicknesses of our samples. We found α_g of single-layer graphene at room temperature to be negative (i.e. graphene shrinks when heated), in the range of $\alpha_g = (-5 \ldots -1) \times 10^{-6}$ K^{-1}, close to the theoretical expectation of $\alpha_g = -3.7 \times 10^{-6} K^{-1}$[Mounet and Marzari, 2005], and smaller in magnitude than the previously reported data for suspended graphene devices[Chen et al., 2009; Singh et al., 2010; Bao et al., 2009]. For double- and triple-layer graphene we determine near-zero $|\alpha_g| < 7 \times 10^{-7} K^{-1}$, close to the value $\alpha_g = -1.2 \times 10^{-6} K^{-1}$ for the in plane coefficient of thermal expansion of bulk graphite[Mounet and Marzari, 2005]. From Au/1xGr devices, we can only estimate the range of the thermal expansion coefficient of single layer graphene on gold, $-8 \times 10^{-6} K^{-1} < \alpha_g < 0$, due to the large uncertainty in the material parameters of gold.

Graphene's large negative coefficient of thermal expansion α_g is a consequence of the two dimensional nature of graphene and is related to the contribution of the of the out-of-plane phonon modes (Lifshitz membrane effect)[Mounet and Marzari, 2005]. In graphite these modes are quenched by the interlayer van der Waals interaction leading to a less negative α_g[Mounet and Marzari, 2005]. The affinity of the thermal expansion coefficients of graphene attached to the substrate to the theoretical expectation of α_g for a pristine suspended graphene membrane suggests that the coupling between graphene and the SiN_x substrate is relatively weak. Surprisingly, the small magnitudes of α_g that we observe in double- and triple- layer devices may indicate that the coupling between graphene layers and hence the suppression the out-of-plane modes in such devices is stronger than that in graphite.

We confirmed the validity of our mechanical model, equations III.1 and III.2, and the accuracy of the tabulated values for substrate material parameters $E_s, \nu_s, \alpha_s(T)$ by fabricating and measuring multiple test devices. First, we fabricated suspended SiN_x cantilevers *without the graphene layer* on top of it, and observed

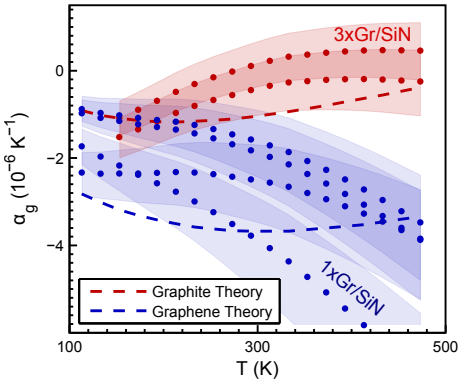

Figure III.7: **Extracting the thermal expansion of graphene on substrates.** Linear thermal expansion coefficient α_g vs. temperature T of single layer (blue circles) and three layer (red circles) graphene, as measured from multiple 1xGr/SiN$_x$ and 3xGr/SiN$_x$ devices. The shaded regions represent the uncertainty in α_g due to the uncertainty in the material parameters of our cantilevers, the blue and red dashed lines are theoretical expectations for α_g of graphene and graphite respectively [Mounet and Marzari, 2005].

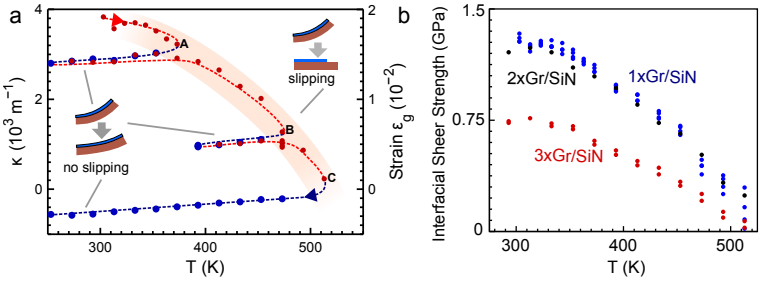

Figure III.8: **Probing adhesion of the graphene silicon nitride interface** a) Slipping of graphene on the silicon nitride cantilever is readily apparent in the hysteretic behavior of curvature. For a given curvature there is a there is a critical temperature where the graphene begins to slip. b) Interfacial shear strength and critical strain ε_{crit} that the 1xGr/SiN interface supports as a function of temperature.

that these cantilevers are flat, as expected. Second, we examined some of the Au/1xGr cantilevers where the graphene layer was removed by exposing the devices to ozone atmosphere. Such cantilevers also remained flat in the entire range of measurement temperatures. Third, we fabricated SiN$_x$/Au cantilevers and confirmed that their temperature-dependent curvature follows equations (III.1) and (III.2). Finally, we perform finite element modeling of the cantilever geometry used in the experiments and confirm that the computed height profile $Z(X)$ is within 3% of the profile predicted by equation III.1.

III.5 Adhesion

Having explored the non-hysteretic behavior of the graphene cantilevers, we now turn to the hysteretic temperature behavior (Fig. 3a,c). Our key observation is that it occurs when the strain in graphene exceeds a critical strain ε_{crit}, which is temperature dependent.

Indeed, when $\varepsilon_g < \varepsilon_{crit}$ the cantilevers bend up and down according to equations III.1 and III.2 as the devices are heated and cooled (Fig. 3d, red and blue data points respectively). However, when $\varepsilon_g > \varepsilon_{crit}$ – such as in the devices immediately following fabrication – the curvature of the cantilevers *decreases* when they are heated (Fig. 3c, red points), contrary to the predictions of equations III.1 and III.2, and does not return to the same value upon cooling (Fig. 3c, blue data points).

We interpret the decrease in strain when $\varepsilon_g > \varepsilon_{crit}$ as graphene slipping along the substrate. When $\varepsilon_g > \varepsilon_{crit}$ the force due to strain exceeds the force acting on graphene due to the friction between graphene and the substrate. At larger strains, graphene delaminates from the substrate and relieves its strain by slipping. This is manifest by straitening of the cantilever or, equivalently, curvature decreasing with temperature $d\kappa/dT < 0$.

We measure the critical strain ε_{crit} as a function of T by heating and cooling the same devices multiple times to gradually increasing temperatures and determining the onset of the slipping behavior (right axis of Fig. 4b; the original data in Supplementary Materials). We now use the measured values of ε_{crit} to roughly estimate the frictional forces between graphene and the substrate. To do so, we note that in order for graphene to slip, the local shear stress in graphene should become larger than the stress due to frictional forces, as quantified by the interfacial shear strength (IFSS) of the graphene/substrate interface. To obtain the numerical estimate of IFSS, we find the maximum shear stress in graphene in 1xGr/SiN, 2xGr/SiN, and 3xGr/SiN devices using finite element analysis.

As expected, we find that the stress is concentrated at the end of the cantilever. Our data reveal a large IFSS of ~ 1 GPa for the 1xGr/SiN devices at room temperature (Fig. 4b). There is a clear weakening of the graphene/substrate friction with temperature that may be related to the weakening of chemical bonds attaching graphene to the substrate we increased T. In light of IFSS we can understand the lower strain observed in the Au/Gr cantilevers as being related to a lower IFSS of the graphene/gold interface. Finally, the IFSS we estimate for graphene on silicon nitride is large and perhaps related to graphene's large adhesion energy[Koenig et al., 2011].

While residues on the graphene may play a role in the strain and IFSS we suspect it is a small effect for the following reasons. First the Young's modulus of PMMA residue is negligible compared to the Young's modulus of either graphene or the substrate. Second, the graphene transfer process results in clean graphene on the side that attaches to the silicon nitride while a majority of the residues from the resist are on the side opposite the interface. Third, while removing residues from graphene resonators does result in changes in strain[Chen et al., 2009], these changes are much smaller than those reported here.

III.6 Conclusion

In conclusion, we note that the reported observations may have several interesting applications. First, the reported significant variation of strain in graphene deposited on different substrates may be exploited towards practical realization of the proposed strain-engineering scheme to control electron properties of graphene[Guinea et al., 2009]. The observed variation in bending in composite graphene cantilevers as a function of temperatures may be used to create novel types of NEMS switches and actuators[Lavrik et al., 2004; LeMieux et al., 2006; Singamaneni et al., 2008], especially bimetallic cantilevers that could be much thinner and therefor more sensitive to small changes in energy of a system enabling sensitive nanocalorimetry. The temperature-induced bending of graphene/gold cantilevers may also explain the failure mechanism in large suspended graphene devices[Bolotin et al., 2008]. Finally, the ability to tune graphene's coefficient of thermal expansion by careful selection of the substrate material and number of graphene layers may be important in designing composite materials based on graphene[Dikin et al., 2007; Potts et al., 2011].

CHAPTER IV

Probing Phonons and Tuning the Band gap of MoS_2

IV.1 Preface

In this chapter I present work on straining monolayers and bilayer of MoS_2 and demonstrate that the strain changes both the Raman and photoluminesence spectra of these materials. Through probing the photoluminesence spectra we were able to show that strain can tune the band gap of MoS_2 and transition the material from a direct band gap material to an indirect band gap material.

Photoluminesence spectroscopy of bilayer samples was done with Jed Zigler while he was a member Richard Haglund's group and the theory was done by Bin Wang while he was part Sokrates Pantelides group. This work has been published previously[Conley et al., 2013].

IV.2 Introduction

Monolayer[1] molybdenum disulfide (MoS_2), along with other monolayer transition metal dichalcogenides ($MoSe_2$, WS_2, WSe_2) have recently been the focus of extensive research activity that follows the footsteps of graphene, a celebrated all-carbon cousin of MoS_2[Wang et al., 2012]. Unlike semimetallic graphene, monolayer MoS_2 is a semiconductor with a large direct band gap[Mak et al., 2010; Splendiani et al., 2010]. The presence of a band gap opens a realm of electronic and photonic possibilities that have not been previously exploited in two-dimensional crystals and allows fabrication of MoS_2 transistors with an on/off ratio exceeding 1×10^8 [Radisavljevic et al., 2011; Lin et al., 2012], photodetectors with high responsivity[Yin et al., 2012], and even LEDs[Sundaram et al., 2013]. Moreover, the direct nature of the band gap causes MoS_2 to exhibit photoluminescence at optical wavelengths[Mak et al., 2010; Splendiani et al., 2010] with intensity that is tunable via electrical gating[Newaz et al., 2013; **?**; Mak et al., 2013]. Finally, strong Coulomb interactions between electrons and holes excited across the band gap of MoS_2 lead to the formation of tightly bound excitons that strongly affect the optical properties of this material[Ross et al., 2013; Mak et al., 2013].

It has been well established that straining a two dimensional material shifts its phonon modes, allowing a simple method to detect strain in these materials. These shifts, that are due to the anharmonicity of molecular potentials, can be probed with micro-Raman spectroscopy[Huang et al., 2009; Mohiuddin et al., 2009]. Very recently, it has been proposed that mechanical strain can strongly perturb the band structure of MoS_2. It has been predicted that straining MoS_2 modifies the band gap energy and the carrier effective masses. Moreover,

[1] Monolayer in this paper refers to one *molecular* molybdenum disulfide (MoS_2) layer, or one layer of molybdenum atoms sandwiched between two layers of sulphur atoms. It is also sometimes refered to as trilayer MoS_2.

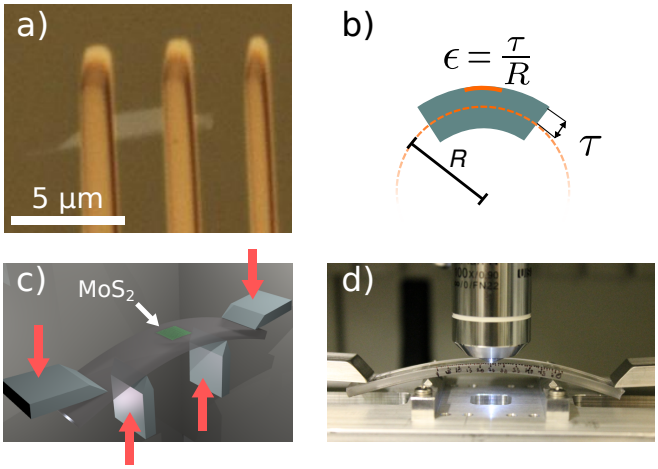

Figure IV.1: **Straining MoS_2 devices** (a) Optical image of a bilayer MoS_2 flake with titanium clamps attaching it to SU8/polycarbonate substrate. (b,c) Schematic of the beam bending apparatus used to strain MoS_2. (d) Photograph of bending apparatus with MoS_2 under strain.

at strains larger than 1% the lowest lying band gap changes from direct to indirect.[Lu et al., 2012; Pan and Zhang, 2012; Yue et al., 2012; Li, 2012; Scalise et al., 2012; Shi et al., 2013]. It has been suggested that strain engineering of the band structure of MoS_2 could be used to increase carrier mobility of MoS_2, to create tunable photonic devices and solar cells[Feng et al., 2012], and even to control the magnetic properties of MoS_2[Lu et al., 2012; Pan and Zhang, 2012]. While strain perturbs the band structure of all materials, two-dimensional materials such as MoS_2 can sustain strains greater than 11%[Bertolazzi et al., 2011], allowing exceptional control of material properties by strain engineering.

Here, we investigate the influence of uniaxial tensile strain from 0% to 2.2% on the phonon spectra and band gaps of both monolayer and bilayer MoS_2, by employing a four point bending apparatus (Fig. IV.1). First, with increasing strain, for both mono- and bilayer MoS_2 we observe splitting of the Raman peak due to the E' phonon mode into two distinct peaks that shift by 4.5 and 1 cm^{-1}/% strain. Second, a linear redshift of 45meV/% strain of the position of the A peak in photoluminescence for monolayer MoS_2 (53meV/% strain for bilayer MoS_2) indicates a corresponding reduction in band gap energy of these materials. Finally, we observe a pronounced strain-induced decrease in intensity of the photoluminescence of monolayer MoS_2. Our modelling and first-principles calculations indicate that this decrease is consistent with a transition of an optical band gap of MoS_2 from direct to indirect at $\sim$1% strain, while the fundamental (or transport) band gap remains direct in the investigated regime of strain. These results have been simultaneously reported by several other research groups[He et al., 2013; Wang et al., 2013].

IV.3 Fabrication

Fabrication of controllably strained devices starts by mechanically exfoliating[Novoselov et al., 2005] MoS_2 onto a layer of cross-linked SU8 photoresist deposited onto a polycarbonate beam. The number of layers of MoS_2 is verified using Raman microscopy[Li et al., 2012].

In order to explore the high strains in this study we had to clamp the MoS_2 flakes to the substrate to minimize the chance of the flake slipping while under strain. This was done using a shadow mask to define metal clamps on the MoS_2 flakes.

IV.3.1 Shadow Masks

Shadow masks are typically thin metal masks that are etched with a pattern. This mask can then be placed directly onto a substrate and can act in place of resist in microfabrication. The principle advantages of shadow masks over traditional photolithography is that the sample or substrate does not come in contact with the chemicals required for photolithography (which are not compatible with the poly-carbonate substrates we used for the bending experiment) and the relative ease of aligning a shadow mask onto a micron sized device.

Shadow masks are limited by being compatible with a limited number of micro-fabrication procedures. As the shadow mask is only in tenuous contact with the substrate only processes like evaporation or gas phase direct etching are possible while wet etches are completely unsuitable with shadow masks. Shadow masks also offer sever constraints on the geometry of the pattern that can be made with them as the mask must be mechanically stable. This is the same limitation that exists with stencils, yielding the peculiar fonts that stencils require. Shadow masks also have a limited resolution. This resolution is limited by how small of a feature that one can etch in the substrate and how close the shadow mask and substrate can be brought together. The final pertinent limitation is the limited lifetime of an individual shadow mask.

These limitations prevented us from using a traditional metal shadow mask as the minimum resolution (typically greater than 10 microns) is too large for the small flakes that we need to clamp. This lead us to explore making shadow masks out of silicon nitride membranes supported on a silicon substrate using a focused ion beam (FIB), where the thinness, less than 200 nm, of the nitride membrane allows a minimum line width of $\approx$ 1 micron with a pitch of $\approx$ 2 microns. This resolution comes at the price of the limited geometries that can be explored due to the intrinsic stress in these films. No structures besides parallel lines were successfully fabricated and these lines were limited to a length of around 50 microns.

Once the shadow mask is fabricated it is aligned to the sample under an optical microscope. In brief this is done by placing the shadow mask, flat side up, ontop of two pieces of kapton tape supported on two pieces of microscope slide, see figure IV.2. While observing and aligning the sample under the microscope, the poly-carbonate beam with exfoliated MoS_2 is then brought into contact with the shadow mask and the tape

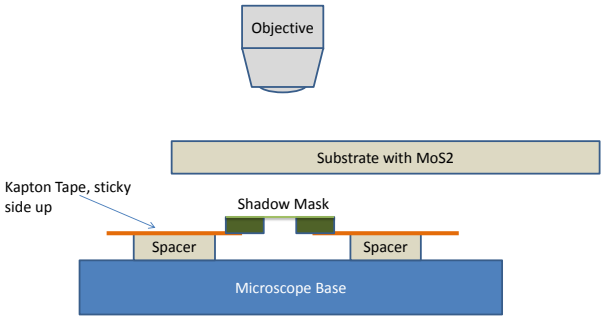

Figure IV.2: **Aligning the shadow mask** The shadow mask is aligned on the poly-carbonate substrate by placing it on top of two pieces of tape. As the substrate is brought into contact with the shadow mask, the tape is pushed up, into sample.

sticks to the polycarbonate beam.

Finally, titanium clamps are then evaporated through a shadow mask(Fig. IV.1a). Uniaxial strain is applied to MoS_2 by controllably bending the polycarbonate beam in a four-point bending apparatus (Fig. IV.1c,d).

IV.3.2 Bending Apparatus

Assuming that as-fabricated exfoliated devices before bending are virtually strain-free[Chen et al., 2009], we can calculate, following section II.6, that upon bending the substrate with radius of curvature R, the induced strain in these devices is $\varepsilon = \tau/R$, where $2\tau = 2$–3mm is the thickness of the substrate (Fig. IV.1b) [Mohiuddin et al., 2009].

I employed a custom built four point bending apparatus. The apparatus consists of two posts and two levers that are actuated by thumb screws. The two posts are adjustable, enabling various distances between the post to enable the user to explore a variety of strains. The radius of curvature of the beam can be calculated by knowing the location of the posts and the levers.

The key of a four point bending apparatus is that it enables one to know the radius of curvature of the bent beam. The radius of curvature is found by assuming that the beam is bent in a circle, following figure IV.3. The beam follows the equation for a circle

$$(x)^2 + (y - y_0)^2 = R^2 \tag{IV.1}$$

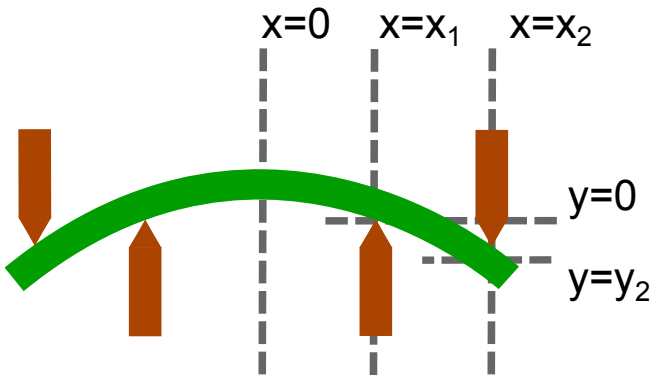

Figure IV.3: **Calculating the radius of curvature** The radius of curvature is completely determined by the geometry of the bending apparatus. By controlling the location of the two posts and the two bending arms, one can bend the beam and induce a known strain on the surface.

where the circle is centered on the x axis and the first point defines zero on the y axis. The goal is to find R which we can do as the posts determine the system such that

$$x_1^2 + (y_0)^2 = R^2 \tag{IV.2}$$

and

$$x_2^2 + (y_2 - y_0)^2 = R^2. \tag{IV.3}$$

Solving this system of equations yields

$$R = \frac{\sqrt{\frac{(x_2^2 - x_1^2)^2}{y_2^2} + y_2^2 + 2x_2^2 + 2x_1^2}}{2} \tag{IV.4}$$

This reduces the challenge of measuring the radius of curvature of the beam to knowing the dimensions of the bending apparatus.

IV.3.3 Devices

While we fabricated many devices in this chapter we focus on four monolayer and three bilayer MoS_2 devices and were properly clamped and showed no sign of slipping. The strained devices are probed with a confocal microscope (Thermo Scientific DXR) that is used to collect both Raman and photoluminescence spectra. We employ a 532nm laser excitation source with average power $\sim$100 μW, which does not damage our samples.

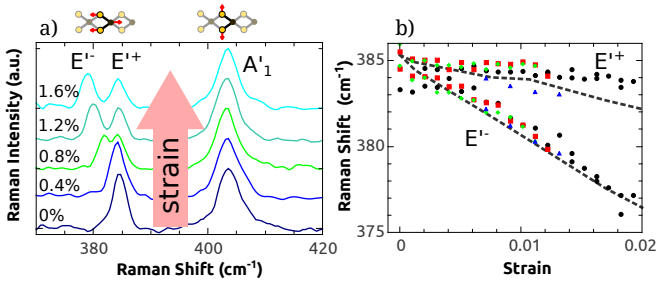

Figure IV.4: **Phonon softening of single layer MoS_2** (a) Evolution of the Raman spectrum as a device is strained from 0 to 1.6%. (b) The peak location of the the E'^{+} and E'^{-} Raman modes, extracted by fitting the peaks to a Lorentzian, as their degeneracy is broken by straining MoS_2. Different colors represent individual devices. Dashed lines are the results of our first-principles calculations after subtraction of 9 cm^{-1} to account for underestimating phonon energies.

IV.4 Raman Spectra of Strain MoS_2

We first investigate the evolution of the Raman spectra of MoS_2 with strain (Fig. IV.4). In unstrained monolayer MoS_2 devices, consistent with previous reports[Lee et al., 2010; Li et al., 2012], we observe the A' mode due to out-of-plane vibrations at 403 cm^{-1} and the doubly degenerate E' mode due to in-plane vibrations of the crystal at 384 cm^{-1}.

With increased strain, the A' peak shows no measurable shift in position while the degenerate E' peak splits into two subpeaks (in contrast to a previous report[Rice et al.,]) that we label as E'^{+} and E'^{-} (Fig. IV.4), as strain breaks the symmetry of the crystal. The A' mode maintains its intensity as strain increases, while the total integrated intensity of the E' peaks now splits between the E'^{+} and E'^{-} peaks. The E'^{-} peak shifts by 4.5 ± 0.3 $cm^{-1}/\%$ strain for monolayer devices and 4.6 ± 0.4 $cm^{-1}/\%$ strain for bilayer devices, while the E'^{+} peak shifts by 1.0 ± 1 $cm^{-1}/\%$ strain for monolayer devices and 1.0 ± 0.9 $cm^{-1}/\%$ strain for bilayer devices, consistent with our first-principles calculations (dashed lines in Fig. IV.4; details of the calculations can be found in the supplementary materials). For applied strain in the range 0–2%, the peak positions shift at nearly identical rates for all measured devices and do not exhibit hysteresis in multiple loading/unloading cycles, indicating that MoS_2 does not slip against the substrate and that the strain does not generate a significant number of defects. Bilayer devices behave in a similar manner but fail, either due to breaking or slipping of the MoS_2, at strains larger than 1%.

The strain dependence of the Raman E' mode enables us to calculate parameters characterizing anaharmonicity of molecular potentials, the Grüneisen parameter, γ, and the shear deformation potential, β:

$$\gamma_{E'} = -\frac{\Delta\omega_{E'^{+}} + \Delta\omega_{E'^{-}}}{2\omega_{E'}(1-\nu)\varepsilon} \tag{IV.5}$$

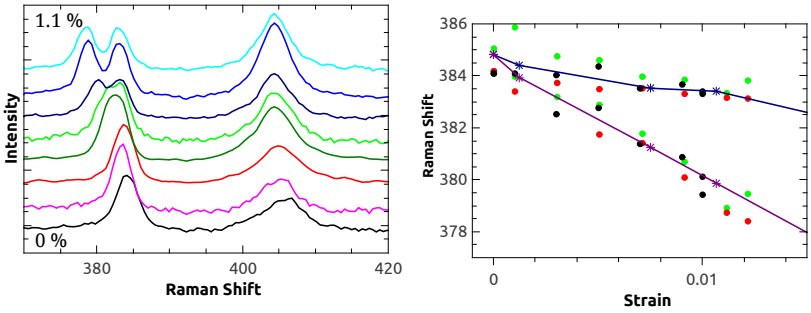

Figure IV.5: **Bilayer Raman Data** a) Raman spectra of a bilayer MoS_2 device for strain levels from 0% to 1.1%. b) Peak locations – obtained by fitting to a Lorentzian – of the E'^{+} and E'^{-} Raman peaks for three different devices.

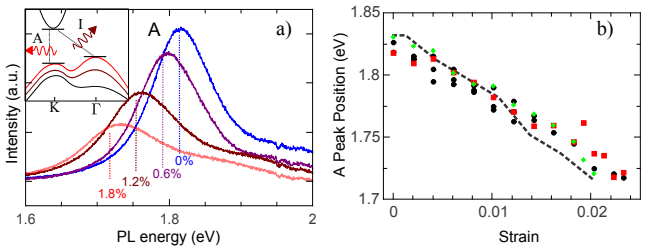

Figure IV.6: **Photoluminescence spectra of strained monolayer MoS_2** (a) PL spectra of a representative monolayer device as it is strained from 0 to 1.8%. Strain independent PL background was subtracted. (b) Evolution of the position of the A peak of the PL spectrum (Lorentzian fits) with strain for several monolayer devices (colors represent different devices) with GW_0-BSE calculations (dashed line) of expected peak position after 25 meV offset. Inset in (a) contains schematic representations of the band structure for monolayer MoS_2 devices that are progressively strained from 0% (black) to ∼5% (maroon) and ∼8% (red).

$$\beta_{E'} = \frac{\Delta\omega_{E'^{+}} - \Delta\omega_{E'^{-}}}{\omega_{E'}(1+\nu)\varepsilon} \tag{IV.6}$$

Here ω is the frequency of the Raman mode, $\Delta\omega$ is the change of frequency per unit strain, and ν is Poisson's ratio, which for a material adhering to a substrate is the Poisson ratio of the substrate, 0.33[Mohiuddin et al., 2009]. This yields a Grüneisen parameter of 1.1 ± 0.2, half that of graphene (1.99)[Mohiuddin et al., 2009] and comparable to that of hexagonal boron nitride (0.95–1.2)[Kern et al., 1999; Sanjurjo et al., 1983]. The shear deformation potential is 0.78 ± 0.1 for both monolayer and bilayer MoS_2.

The evolution of the Raman spectra for bilayer MoS_2 devices with strain is similar to that of monolayer MoS_2. Bilayer MoS_2 exhibits the same rates of change of the Raman peak position as for monolayer MoS_2 within the measurement uncertainty (Fig. IV.5). This yields the same value for the Grüneisen parameter, 1.06 ± 0.2.

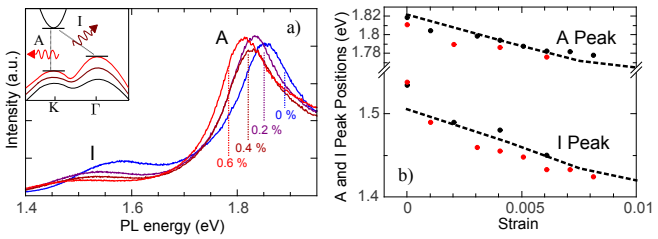

Figure IV.7: **Photoluminescence spectra of strained bilayer MoS_2** (a) PL spectra of a representative bilayer device as strain is increased from 0 to 0.6%. (b) PL peak position versus strain for the A and I peaks of bilayer devices (colors represent different devices) with good agreement to our GW_0-BSE calculations (dashed lines). Inset in (a) contains schematic representations of the band structure for monolayer MoS_2 devices that are progressively strained from 0% (black) to ∼5% (maroon) and ∼8% (red).

IV.5 Photoluminescence of Strained MoS_2

Next, we investigate the evolution of the band structure of MoS_2 with strain through photoluminescence (PL) spectroscopy. The principal PL peak (A peak) in unstrained direct-gap monolayer MoS_2 at 1.82±0.02 eV (Fig. IV.6a) is due to a direct transition at the *K* point (Fig. IV.6a, inset)[Splendiani et al., 2010; Mak et al., 2010]. The B peak, due to a direct transition between the conduction band and a lower lying valence band, is obscured in our devices by background PL of polycarbonate/SU8. The PL spectra of unstrained indirect-band gap bilayer MoS_2 devices are characterized by a similar A peak at 1.81±0.02 eV that originates from the same direct transition, but that is now less intense as it originates from hot luminescence. In addition, we observe an I peak at 1.53±0.03eV (Fig. IV.7a), which originates from the transition across the indirect band gap of bilayer MoS_2 between the Γ and *K* points, (Fig. IV.7a, inset).

Applied strain significantly changes the PL spectra (Fig. IV.6a and IV.7 a). For all measured monolayer devices, the A peak redshifts approximately linearly with strain, at a rate of 45 ± 7 meV/% strain (Fig. IV.6b). For bilayer devices, the A and I peaks are redshifted by 53 ± 10 and 129 ± 20 meV/% strain respectively (Fig. IV.7b). While the intensity of the A peak in monolayer devices decreases to a third of its original size with an applied strain of 2%, in bilayer devices the intensity of this peak is virtually strain-independent (Fig. IV.6a).

To understand our experimental results, we compare them to the results of GW_0-BSE calculations; details are given in supplementary materials. Crucially, these calculations capture the effect of strong electron-electron interactions in MoS_2 leading to the formation of excitons with binding energies significantly exceeding k_BT at room temperature [Cheiwchanchamnangij and Lambrecht, ; Ramasubramaniam, 2012]. This is important because PL spectroscopy probes the optical band gap, the difference between the fundamental (or transport) band gap and the exciton binding energy.

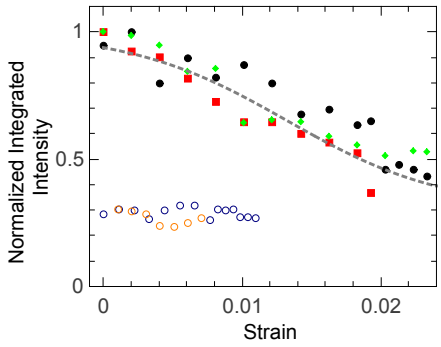

Figure IV.8: **Intensity of strained MoS_2 films** Evolution of intensity of the A peak of strained monolayer MoS_2 (solid shapes) with a fit (dashed curve) to the rate equations consistent with a degenerate direct and indirect optical band gap at 1.3±0.6% strain (supplementary material). PL intensity of bilayer A peak (unfilled circles) with no measurable change in intensity. Each color represents a distinct device.

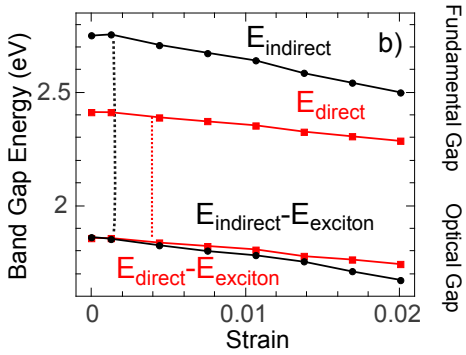

Figure IV.9: **Direct to indirect band gap transition in MoS_2** GW_0 calculations of the fundamental band gaps of strained monolayer MoS_2, with an expected degeneracy at ∼5% strain. Optical band gap calculated by including the exciton binding energy yields a degeneracy at ∼ 0.1%.

The observed redshift of the PL peaks is indicative of strain-induced reduction of band gaps in both monolayer and bilayer MoS_2. Indeed, our GW_0-BSE calculations for a monolayer predict a reduction of the optical band gap at a rate of ∼59 meV/% strain (dashed line in Fig. IV.6b), in close agreement with the measured PL peak shift. In bilayer devices, the calculated rates of reduction for the direct (67 meV/% strain) and indirect (94 meV/% strain) optical band gaps (dashed lines in Fig. IV.7b) are also in close agreement with measured redshift rates for A and I peaks, 53 ± 10 and 129 ± 20 meV/% strain respectively.

IV.6 Intensity of photoluminescence of MoS_2

IV.6.1 Modeling the photoluminescence intensity of strained MoS_2

We model monolayer MoS_2 as a two-level system, Fig. IV.10. One level corresponds to a direct exciton at the *K* point that is responsible for the A photoluminescence peak and the other level corresponds to an

indirect exciton due to a transition between the K and Γ points. The change in PL intensity of monolayer MoS_2 is due to the changing energy difference between these two levels, ΔE with strain ε. To quantitatively describe the variation of PL intensity with strain, we start by writing down simple rate equations for the time dependence of the population densities of direct, n_d, and indirect, n_i, excitons in our two level system, Fig. IV.10[Sánchez-Pérez et al., 2011].

$$\frac{dn_d}{dt} = \Phi_0 - n_d R_d - n_d T_{di} + n_i T_{id} \tag{IV.7}$$

$$\frac{dn_i}{dt} = -R_i n_i + T_{di} n_d - n_i T_{id} \tag{IV.8}$$

Here R_d and R_i are the total radiative and non-radiative recombination rates of direct and indirect excitons respectively, Φ_0 is the photoexcitation rate for direct excitons, and T_{di} and T_{id} are transition rates between direct and indirect excitonic levels. In order to solve these equations we make two assumptions. First we assume that the transition rates are exponentially dependent on ΔE, $T_{di} = Te^{-\Delta E/kT}$ and $T_{id} = T$ when $\Delta E > 0$ and $T_{id} = Te^{\Delta E/kT}$ and $T_{di} = T$ when $\Delta E < 0$[Selg and Kink, 2003]. Second, we assume that the steady-state populations of excitons are constant, $\frac{dn_d}{dt} = \frac{dn_i}{dt} = 0$. Employing these assumptions we find solution to Eqs. IV.7 and IV.8 for n_d:

$$n_d = \frac{\Phi_0}{R_d} \begin{cases} \frac{1}{\frac{R_1}{R_2+1} e^{-\Delta E/kT} + 1} & \text{if } E > 0 \\ \frac{1}{\frac{R_1}{R_2 e^{\Delta E/kT} + 1} + 1} & \text{if } E < 0 \end{cases} \tag{IV.9}$$

where $R_1 = T/R_d$ and $R_2 = T/R_i$.

We now assume that overall photoluminescence intensity of the A peak is proportional to the density of direct excitons, and that ΔE changes linearly with applied strain ε, $\Delta E = \alpha\varepsilon - \beta$ (Fig. 3d). By fitting Eq. IV.9 to the strain-dependent photoluminescence intensity data in monolayer MoS_2 devices (Fig. 4a of the main text) we obtain α=38$\pm$10 meV/% strain, $\beta = 50 \pm 35$ meV, $R_1 = 3 \pm 2$ and $R_2 = 2.8 \pm 2$ (fit plotted as a dashed line in Fig. IV.8.

Despite the large number of parameters being fit, we believe that the results of the fit are in good agreement with our expectations based on the band structure of MoS_2. First, we find the direct and indirect transitions are degenerate at strain $\varepsilon_0 = \beta/\alpha = 1.3 \pm 0.6\%$. This is larger but consistent with the degeneracy at 0.1% from our first-principles calculations. Second, the fitted value for the difference between the direct and indirect transitions at zero strain is 50$\pm$35 meV, also in agreement with the results from our first-principles calculations of 90 meV.

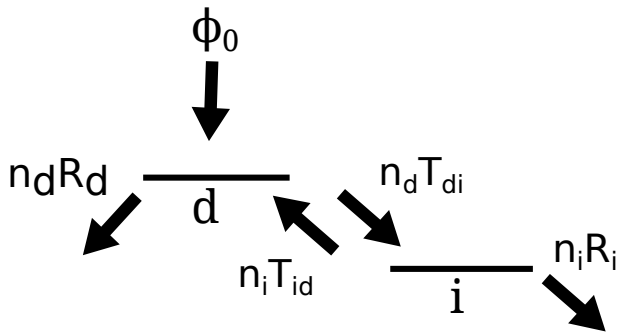

Figure IV.10: **Two level system** Two level system that is solved to determine n_d.

IV.6.2 Experimental photoluminescence intensity of strained MoS_2

We interpret the rapid decrease in PL intensity of monolayer MoS_2 with strain as a signature of the anticipated strain-induced transformation of the *optical* band gap of this material from direct to indirect[Lu et al., 2012; Pan and Zhang, 2012; Shi et al., 2013; Feng et al., 2012]. Indeed, at zero strain the energy difference between the minimum of the conduction band at the K point and the local maximum of the valence band at the Γ point (the indirect gap) is higher in energy than the direct gap at the K point (Fig. IV.6a, inset, black curve). However, we calculate that the indirect gap reduces with strain faster than the direct gap (59 vs. 94 meV/% strain). As a result, if we ignore the effect of excitons, at $\varepsilon \sim 5\%$ the indirect gap overtakes the direct gap and monolayer MoS_2 becomes an indirect-gap material. With excitonic effects included, our calculations indicate that the direct and indirect *optical* gaps (fundamental gaps minus binding energy of corresponding excitons) become degenerate at a much lower strain, 0.1% (Fig. IV.9). We however note that the accuracy of this value sensitively depends on the precise binding energy of the direct and indirect excitons that have not yet been measured experimentally.

As monolayer MoS_2 is strained and transitions from a direct to an indirect band gap material, we expect a marked decrease in the intensity of the A peak, as a majority of the excitons would not reside in this higher energy excitonic state, in good agreement the decrease in intensity in Fig. IV.8. Quantitatively, a simple model describing direct and indirect excitons in monolayer MoS_2 as a two-level system yields an acceptable fit to our experimental data (dashed curve in Fig. IV.8), with a direct-to-indirect band gap transition at $1.3 \pm 0.6\%$ strain (details in supplementary information).

The observed PL spectra warrant two more comments. First, while for strains where the indirect band gap of monolayer MoS_2 is lower in energy than the direct band gap, we do not observe a peak corresponding to an indirect transition in its PL spectrum. This is likely due to the much smaller intensity of the indirect photoluminescence compared to the intensity of hot luminescence of the A peak. Second, in the range of

strains from 1.3–5%, monolayer MoS_2 enters a curious regime where its fundamental band gap is direct, while the optical band gap is indirect.

IV.7 Conclusion

In conclusion, we have observed strain-induced phonon softening, band gap modulation and a transition from an optically direct to an optically indirect material in strained MoS_2 samples. These observations support a view of strain engineering as an enabling tool to both explore novel physics in MoS_2 (and other two-dimensional transition metal dichalcogenides such as $MoSe_2$, WS_2, WSe_2) and to tune its optical and electronic properties. An interesting avenue of research would be to explore the regime of degenerate direct and indirect bands – that play key roles in a plethora of spin-related properties of the MoS_2[Mak et al., 2012; Zeng et al., 2012]. Among the potential applications of the strain-dependent photoluminescence of MoS_2 and its cousins are nanoscale stress sensors and tunable photonic devices – LEDs, photodetectors, and electro-optical modulators.

CHAPTER V

Graphene as a Two Dimensional Entropic Spring

V.1 Introduction

Graphene inhabits a unique position in the material world. On the one hand it can be characterized as a classic hard condensed matter system, with its exceptional crystallinity and commensurate mechanical strength[Lee et al., 2008]. On the other hand it is a classic soft condensed matter system as it is an atomically thin material where entropy should dominate its material properties. Both of these regimes are manifest when probing the Young's modulus of graphene. At high stresses, graphene behaves like bulk materials and one measures a Young's modulus due to stretching interatomic bonds[Bunch et al., 2008; Lee et al., 2008]. However, at the low stress regime where flexural phonons are large and graphene acts like an entropic spring. The presence of an entropic spring constant is disruptive in the graphene community as multiple studies[Singh et al., 2010; Chen et al., 2009] have assumed that the larger spring constant of strained graphene is applicable in the low strain regime, requiring a reanalysis of their results.

V.2 In-plane Stiffness of Graphene

Graphene's Young's modulus is of principle importance for understanding basic material properties and designing and understanding future graphene based MEMS devices. Due to this critical importance many studies have directly probed the Young's modulus of this material.

The first challenge of probing the Young's modulus is in the very definition of Young's modulus. The Young's modulus of a material is

$$\varepsilon = \sigma E \tag{V.1}$$

where ε is the strain, σ is the stress, and E is the Young's modulus. E is poorly defined in a two dimensional material, as stress $\sigma = F/A$ is the force over the area, and thickness is a nebulus quantity in a two dimensional material. Defining the thickness of a two dimensional material is non-trivial, with at least three valid definitions that give different answers. One common way to define the thickness of a two dimensional material is to take the three dimensional material from which the two dimensional material is derived, graphite in the case of graphene, and extract the interlayer spacing and define that as the thickness of a monolayer. Another plausible route is if one assumes that as an atomically thin material, the thickness is the Bohr radius of a carbon atom. This however is not a concrete definition of thickness as is only a distance that some of the electrons are from the carbon atom. A more pragmatic route would be to measure the thickness of the

sheet with an AFM. However, the measured height of a monolayer layer of graphene can vary dramatically depending on the substrate that graphene is on, and the mode used to image graphene.

Due to the challenge associated with defining thickness of a two dimensional material, we instead turn to a two dimensional proxy of the Young's modulus, in-plane stiffness. In plane stiffness is

$$\varepsilon = \eta M \tag{V.2}$$

where η is the line pressure, defined as force over length, and M is the in-plane stiffness.

Several groups have measured this in-plane stiffness. The first attempt to extract this in-plane stiffness of graphene was done using graphene mechanical resonators[Bunch et al., 2007]. By measuring the resonant frequencies of graphene resonators versus their length and thickness, they were able to show that the resonances were consistent with an in-plane stiffness of 340 N/m, the expected in-plane stiffness of graphite. A follow up study by the same group more directly probed the in-plane stiffness of graphene using a bulge test. They pressurized one side of a graphene sheet and measured the deflection of the pressurized sheet. Experimental limitations only allowed them to collect data for devices under large strain but they showed a clear in-plane stiffness of 390 N/m[Bunch et al., 2008].

Another attempt[Lee et al., 2012], that on the surface would appear to be more sensitive to low strain effects, using the same bulge test, but employed Raman spectroscopy to directly measure the strain. This method is incapable of probing the entropic regime as Raman is only sensitive to interatomic stretching and cannot be used to observe the changes in strain due to pulling out the thermal ripples.

Perhaps the most definitive measure of the in-plane stiffness of graphene was done by straining the film with an AFM tip and measuring the resultant deflection. By straining films up to 30% strain they showed that graphene has an in-plane stiffness of 340 N/m and behaves nonlinearlly at higher strains[Lee et al., 2008].

This work has been followed up by another group that both verified the in-plane stiffness of 340 N/m but also showed that the in-plane stiffness can be modified by inducing defects into the material. By damaging the sample with argon they were able to increase the in-plane stiffness to as high as 550 N/m[López-Polín and Gómez-Navarro, 2014].

More curiously, Bao et al[Bao et al., 2012] measured the in-plane stiffness using a strip geometry, where graphene is clamped on two ends like the device shown in figure II.3. Graphene is then electrostatically pulled down while observed in an SEM. They were able to see actuation of the graphene device and saw two distinct regimes. In the first regime they saw the graphene in a soft phase that they attributed to slipping. However, this explanation is unlikely as the motion was not hysteretic. After annealing their devices they saw that they followed the more traditional in-plane stiffness of 340 N/m.

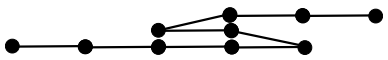

Figure V.1: **An Ideal Chain** The simple model of an ideal chain can be used to calculate the entropic forces in one dimension. This image represents just one possible microstate that this ideal chain can inhabit.

These studies together point to graphene's in-plane stiffness being dominated by the interatomic bonds. However all the studies, with the possible exception of Bao et al[Bao et al., 2012] before annealing, were limited to high strains. In the low strain regime, entropic effects can dominate, leading to a much lower in-plane stiffness.

V.3 Entropic Spring in One Dimension

One generally thinks of a material's spring constant as defined by the stiffness of its molecular bonds, and while this can be true for crystalline bulk materials it inadequately describes a rather common soft material, the rubber band. The rubber band can be considered a one dimensional material on the molecular level, as it consists of a collection of long polymer chains. These polymer chains are not all perfectly aligned and straight, but all jumbled up to minimize the entropy of each individual polymer chain. When one stretches a rubber band one elongates these polymer chains. Hence when pulling against entropy the material is being pulled into a less probable state instead of pulling against intermolecular bonds. This is why one can stretch rubber bands 100% while a typical hard material fails at 2% strain.

A simple model for an entropic spring, following the lecture notes from Ben Schwartz, is a one dimensional ideal chain. Figure V.1 shows one possible microstate of an ideal chain, of N units, and total m turns. For this ideal chain of nine units that is 5 units wide, it is one of 126 microstates with this end to end distance. In general the number of microstates, Ω, for each macrostate is

$$\Omega = \frac{N!}{m!(N-m)!}, \tag{V.3}$$

This can be approximated as a normal distribution if $N >> 1$ and $m - N/2 << N$, yielding

$$\omega \approx \sqrt{\frac{2}{N\pi}} e^{-\frac{(m-N/2)^2}{N/2}} 2^N \tag{V.4}$$

It is convenient to cast this in terms of length of the chain, x, where $k = m - (N-m) = 2m - N$

$$\omega = \sqrt{\frac{2}{\pi N}} 2^N e^{-\frac{x^2}{2N}} \tag{V.5}$$

The entropy of the chain is then

$$S = k_b \ln(\sqrt{\frac{2}{\pi N}} 2^N e^{-\frac{x^2}{2N}}) \tag{V.6}$$

From this we can calculate the Helmholtz free energy,

$$A = -ST \tag{V.7}$$

and note that $F = dA/dx$. This yields a force of

$$F = k_b T x/N \tag{V.8}$$

This simple model captures several important facets about entropic springs. Namely that the spring constant of an entropic spring is proportional to temperature, and the spring constant scales with the size of the chain. We expect both of these findings to translate over two-dimensional materials.

V.4 Entropic Springs in Two Dimensions

The elastic nature of an entropic sheet can also be derived from a phenomenological model following previous work focusing on biological membranes[Helfrich and Servuss, 1984]

The elastic energy per unit area of a sheet under curvature is

$$U_C = \frac{1}{2}\kappa(c - c_0)^2 \tag{V.9}$$

where κ is the bending modulus, c is curvature and c_0 is the spontaneous, or built in, curvature of the membrane.

If we have a membrane with area A and periodic boundary conditions we can decompose the ripples of the sheet into modes u

$$u(r) = \sum_q u_q e^{iqr} \tag{V.10}$$

where $q = 2\pi/A^{1/2}(m,n)$ where m and n are integers.

If the height of the ripples is small, we can approximate the curvature, c as $\nabla^2 u$. This allows us to calculate the energy associated with a set of modes as

$$U_c = \frac{1}{4} A \kappa q^4 |2u_q|^2. \tag{V.11}$$

To calculate how a sheet will change in size due to ripples we assume we have a well behaved sheet that

follows

$$|\nabla u| = \tan\phi << 1 \tag{V.12}$$

where ϕ is the tilt angle of the membrane with respect to the overall plane of the membrane.

Ripple in the sheet will change the area, A of the sheet by

$$\Delta A = \cos\phi - 1 \approx \phi^2/2 \approx -\tan(\phi)^2/2 = (\nabla u)^2/2 \tag{V.13}$$

This leads to

$$(\Delta A)_q = -\frac{1}{4} A q^2 |2u_q|^2 \tag{V.14}$$

The energy cost of pulling out these wrinkles is then just

$$\sigma(\Delta A)_q \tag{V.15}$$

The mean square amplitudes of each mode can be found using the equipartition theorem, with each mode receiving one $k_b T$ of energy.

$$< |u_q|^2 >= \frac{kT}{A(q^4\kappa + q^2\sigma)} \tag{V.16}$$

In order to find the total change in area we have to sum up the effect of all the modes. This is done by

$$\sum_q \rightarrow \frac{A}{2\pi} \int 2\pi q dq \tag{V.17}$$

If we integrate from the minimum bending length, a, to A[1] this leads to

$$\frac{\Delta A}{A} = \frac{kT}{8\pi\kappa} \ln \frac{\sigma a^2}{\kappa\pi^2} + \frac{1}{\lambda}\sigma \tag{V.18}$$

where λ is the atomic in-plane stiffness.

This equation does not yield an analytic entroptic in-plane stiffness. However, it is a simple matter to numerically calculate the in-plane stiffness, as shown in figure V.2. This is done by using equation V.18 to generate stress strain curves.

At low strains, the entropic in-plane stiffness is less than 10 N/m and increases until it plateaus at the atomic in-plane stiffness of graphene. Also, the entropic term is temperature dependent, approaching the atomic in-plane stiffness at low temperatures, as the flexual modes are frozen out, see figure V.3

[1] Integrating to A is a questionable practice as the ripples will eventually self limit[Nelson and Peliti, 1987]. However it provides a clean closed solution and for the purpose of this document is sufficient

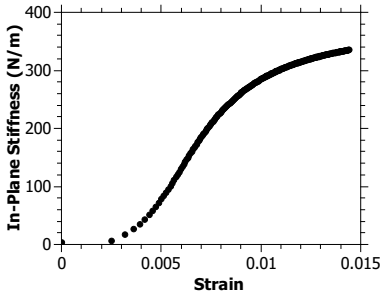

Figure V.2: **In-plane stiffness of an entropic membrane** In-plane stiffness of a 3 by 3 micron membrane with both entropic and standard in-plane stiffness at 300K. At around 1% strain, the sheet transistions from a soft material dominated by entropic effects to a hard material dominated by the carbon-carbon bond stiffness.

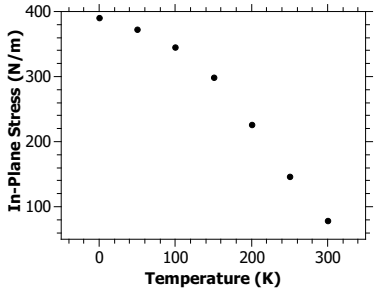

Figure V.3: **In-plane stiffness of an entropic membrane versus temperature** In-plane stiffness of a 3 by 3 micron membrane with both entropic and standard in-plane stiffness at 0.05% strain. At low temperatures and the fluctuations are frozen out, the in-plane stiffness aproaches that of graphite.

V.5 Bulge Test

The in-plane stiffness of a membrane can be extracted through the traditional bulge test[Vlassak and Nix, 1992]. In the bulge test, a pressure is applied to a freestanding film and the deflection of the membrane is measured, enabling one to extract both the Young's modulus and Poisson ratio of a thin film. In the following section the basic theory of the bulge test for two dimensional materials is derived following a standard procedure[Wu et al., 2004].

The stress on a circular membrane under uniform pressure is

$$\eta = \frac{\Delta P R}{2} \tag{V.19}$$

where η is the 2D stress, ΔP is the pressure on the membrane, and R is the radius of curvature of the bent membrane. Referencing figure V.4, we can turn this into more natural coordinates by noting that

$$R = \frac{h}{2} + \frac{a^2}{2h} \tag{V.20}$$

and by ignoring the $h/2$ term as $h << a$ we can then rewrite equation V.19 as

$$\eta = \frac{\Delta P a^2}{4h}. \tag{V.21}$$

The strain that the membrane is under can also be found from basic geometry

$$\varepsilon = \frac{2h^2}{3a^2}. \tag{V.22}$$

Equipped with both the stress and strain we note that in two dimensions

$$\eta = M\varepsilon + \eta_0 \tag{V.23}$$

where η_0 is the built-in stress of the film. Putting these equations together yields

$$\Delta P = \frac{4\eta_0}{a^2} d + \frac{8}{3}\frac{M}{a^4} d^3. \tag{V.24}$$

Experimentally, pressure is applied electrostaticly (see section II.5), yielding a pressure of

$$\Delta P = \frac{1}{2}\frac{\varepsilon_0}{z^2} V_{gate}^2 \tag{V.25}$$

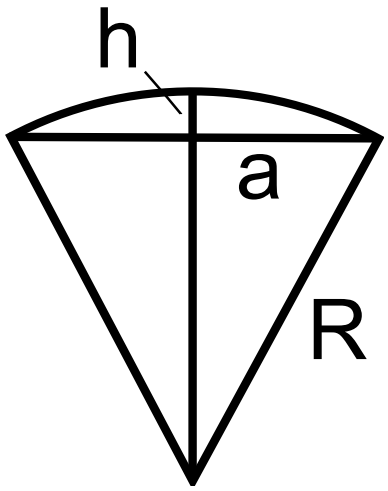

Figure V.4: **Geometry for bulge test** As the membrane is pulled down by a pressure we assume that the resulting film follows a circle. R is the radius of curvature of the circle that the membrane forms, a is the radius of the hole, and h is the center displacement of the membrane.

where ε_0 is the permitivity of free space, z is the distance to the gate, and V_{gate} is the voltage applied between graphene and the gate. This leads to the experimentally applicable result of

$$V_{gate} = \sqrt{\frac{2z^2}{\varepsilon_0}(\frac{4\eta_0}{a^2}d + \frac{8}{3}\frac{M}{a^4}d^3)}. \tag{V.26}$$

V.6 Experimental Setup

Attempting to measure the entropic in-plane stiffness of graphene with the bulge test puts several rigorous constraints on the design of these devices. We need to explore these membranes under very small forces with minimal perturbation of the membrane with our experimental apparatus. Previous studies have focused on pressure gradients by putting gases with different pressures on either side of the membranes. This enables larger pressures, but cannot be used for the smaller pressures required to probe the entropic effect of the stiffness of graphene.

By electrostatically pulling down graphene membranes we can probe the stress strain relation and much smaller pressures. Typical electrostatic pressures that are applied are around 100 Pascals, in contrast to typical pressures of 10^5 Pascals used in previous studies. This much smaller pressure enables the exploration of a new regime previously unattainable.

Previous groups have probed these films with an AFM. However we could not use an AFM to probe large films as we found that they bent under the force of the cantilever and we could not decouple the effect of the AFM versus another force with the very small electrostatic forces involved in these experiments. One group

managed to probe these films with an SEM, however this is an exceedingly challenging manner to probe changes in heights, with poor sensitivity.

Instead we probe these samples using an interferometric profilometer (discussed in section II.3), a non-contact method to probe a materials vertical topography with angstrom resolution. However, it adds to the challenge that the graphene film must be optically distinct from the gate in order to resolve them independently, in our case requiring a separation greater than 1 micron. This required non-standard fabrication techniques in order to make these devices.

The remaining section is split into two subsections. The first section covers fabrication of the devices that were used to measure the entropic nature of graphene. The second subsection is devoted to the air gates, used the actuate the devices.

V.6.1 Device Fabrication

In order to make graphene devices that were compatible with the optical profilometer we needed a graphene-gate spacing greater than 1 micron. This limitation caused us to build the graphene device and the gate, called an air gate, separately, and then join these two devices together to make the measurement apparatus. This section highlights the fabrication of the graphene part of the apparatus.

Suspended graphene membranes were made by transferring CVD graphene onto gold coated patterned silicon nitride membranes.

An outline of the fabrication scheme is shown in figure V.5. Silicon nitride membranes were fabricated at the Center for NanoPhase Material Science (CNMS) at Oak Ridge National Laboratory. Fabrication was done by growing a low stress silicon nitride membrane (500 nm to 1 micron in thickness) using a low pressure CVD process (Tystar Furnace). Holes were patterned into low stress silicon nitride films using standard photolithography. Then the silicon nitride on the back side of the wafer was also patterned and the wafer is etched in KOH. The KOH etch etches through the silicon all the way to the silicon nitride film on the other side, forming a suspended silicon nitride membrane. Gold, 50-90 nm, was then evaporated on the silicon nitride membranes.

Graphene was grown and transferred following work previously published[Vlassiouk et al., 2013]. This graphene has been shown to be of exceptional quality with individual grains larger than 100 microns. The key difference in the transfer from the reference is that the gold coated silicon nitride membranes are exposed to an oxygen plasma for one minute before graphene is transferred onto the substrate. Figure V.6 shows the approximate yield of the transfer process.

After the transfer process, graphene is under strain, making the measurements challenging. Simply annealing the graphene coated membranes at 350 C for 30 minutes in an H_2/Ar environment relieves much of

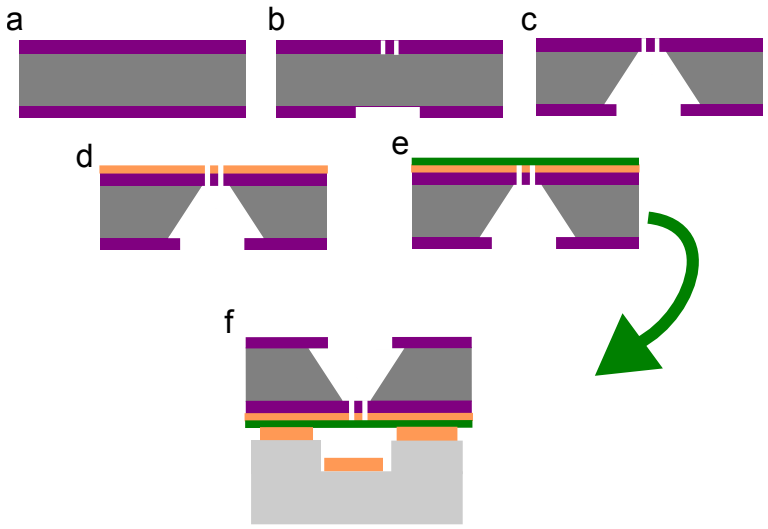

Figure V.5: **Device to probe graphene stiffness** Discription of the fabrication method used to make graphene membranes that can be probed under the optical profilometer. Starting with a silicon wafer coating with silicon nitride (a), we pattern the silicon nitride on both sides of the wafer (b) and then etch the wafer in KOH (c). We take the now etched wafer and evaporate gold onto the surface (d) and then tranfer graphene onto these structures. The resulting device is then transfered onto an air gate.

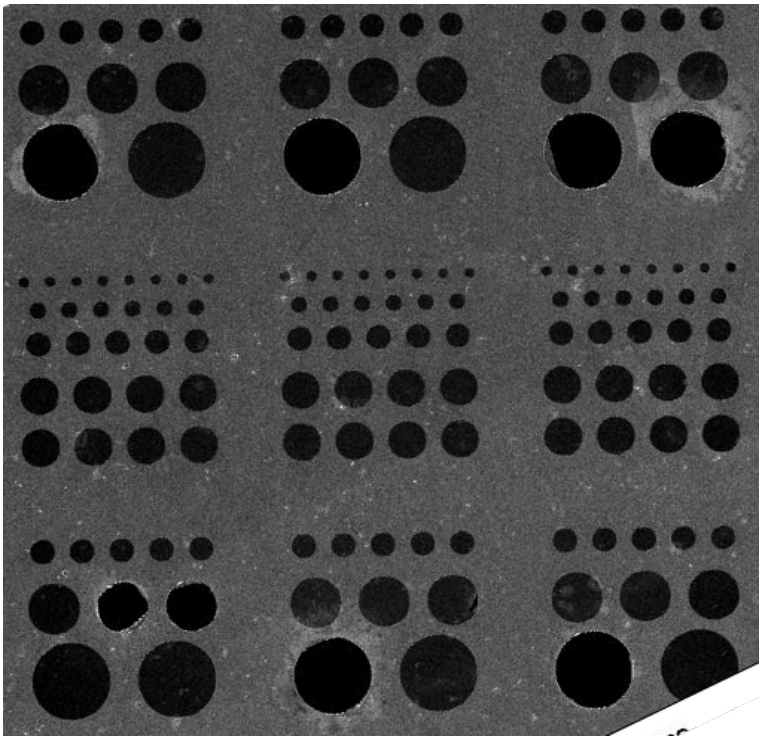

Figure V.6: **Graphene transfer on a silicon nitride membrane** SEM image of a silicon nitride membrane after graphene has been transferred onto the membrane. While not all the holes have intact graphene, most do, including about half of the holes 30 microns in diameter. The largest holes in this image are 30 microns in diameter.

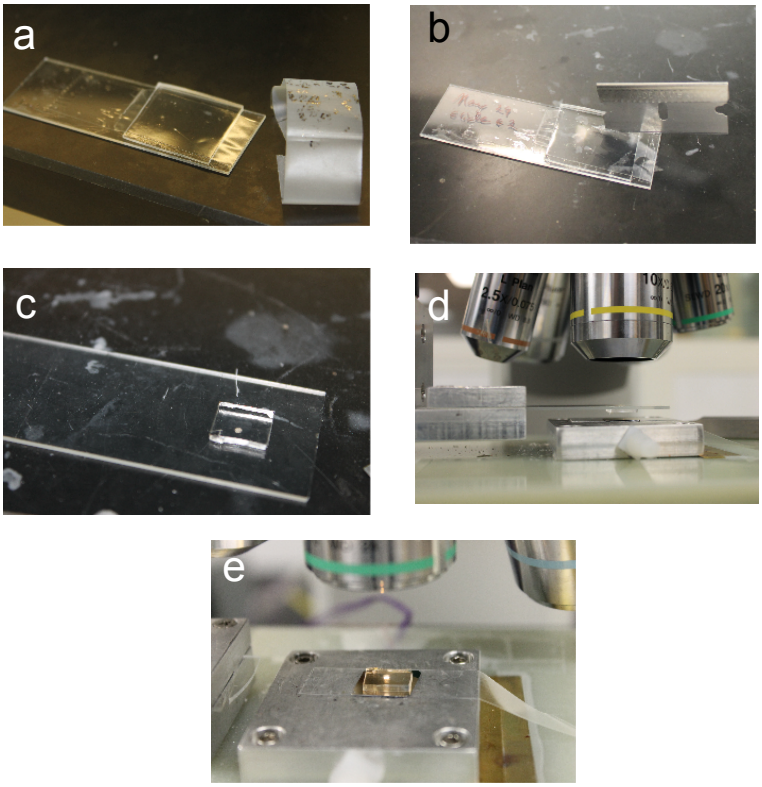

Figure V.7: **Exfoliated graphene transfer on a silicon nitride membrane** Process to transfer exfoliated graphene onto a silicon nitride membrane. a) First one exfoliates graphene onto a PMDS, transparent tape, elvacite stack. Then once a viable flake of graphene is identified, a small piece of the stack is cut out, b), and placed into an new glass slide c). d) The glass slide and oxygen plasma cleaned silicon nitride membrane are put in a custom transfer stage and aligned and pressed together. After heating to 75 C the glass slide is removed, e), and the sample is put in acetone, removing the elvacite stack from the membrane, transfering the graphene onto the membrane.

the strain and is a crucial step prior to measurement.

Graphene membranes can also be made using exfoliated graphene in order to explore the mechanics with the highest quality samples possible. This is done by exfoliated graphene onto a transfer slide and then transferring the graphene onto the membrane. Transfer slide are made by placing a piece of PDMS onto a glass slide and covering the PDMS with clear tape. Elvacite is then spun onto the tape. At this point the slides are ready for exfoliation of graphene, see figure V.7 a.

Graphene exfoliation onto the elvacite must be done very lightly or one rips off the elvacite. So the tape is lightly placed down on the substrate and then pulled off over a matter of several minutes. Then the glass slide, PDMS, tape, elvacite stack is examined under the microscope in search of monolayer graphene.

Graphene monolayers are identified using contrast and verified with Raman spectroscopy. The elvacite stack is then cut out into a smaller piece and placed onto a new slide. This is to preserve the integrity of the

silicon nitride membrane during the transfer process. If one tries to use a full width stack, one either does not get good contact on the nitride membrane and nothing transfers, or one rips off the delicate membrane from the silicon frame. By cutting a small piece out of the elvacite stack and gently placing it on a new slide, the PDMS layer delaminates from the glass slide during transfer, see figure V.7 e, leaving the silicon nitride membrane intact.

The transfer is done by aligning the graphene flake onto the holes in the silicon nitride membrane under the optical microscope, see figure V.7d, and then pressing the two pieces together. Once contact has been achieved, the stage is heated up to 75 C and the temperature is maintained for five minutes. After five minutes the glass slide is lifted up, transferring the graphene and the elvacite PDMS stack, see figure V.7e.

V.6.2 Air Gates

The graphene on silicon nitride is impressive, figure V.6, however it cannot be used to probe the in-plane stiffness of graphene as one cannot apply an electric field to these devices. To apply an electric field to the graphene, the silicon nitride membranes are placed face down onto a second wafer that we refer to as an air gate.

Air gates consist of three electrodes, two outer electrodes that enable one to bias the graphene, and a third electrode in the center that is recessed and used to gate the graphene. The setup enables one to place a silicon nitride membrane facedown on the air gate and apply a bias to the graphene and to a gate.

Successful air gates are made on completely insulating substrates with patterned, recessed electrodes. Attempts to make air gates on conducting substrates with a thin film insulator proved unsuccessful as when the silicon nitride membrane and the air gate are pressed together, the silicon nitride membrane invariably crushes through the thin film oxide, creating a gate leak.

Another major issue with air gates is that the center gate electrode must be sufficiently recessed so that no crud on the silicon nitride membranes can bridge the membrane and the gate, shorting the gate and causing a gate leak. In practice this means that the gate must be recessed several microns.

Air gates were made by etching trenches into a silica wafer. A silicon nitride etch mask was grown onto the air gate by PECVD followed by another layer of PECVD silica. The wafer was etched down to the etch mask, and then the etch mask was removed via a dry etch. Once the topography of the gate was established, gold was evaporated to make the electrodes.

If the distance between the device and the gate was too small, significant gate leakages occurred. These leaks are assumed to originate from crud on the silicon nitride membranes from the transfer process. This crud probably contacts the gate, creating leaks. In order to overcome this we used 8 micron thick titanium foil spacers on the air gate to control the distance between the gate and device. For a majority of samples 20

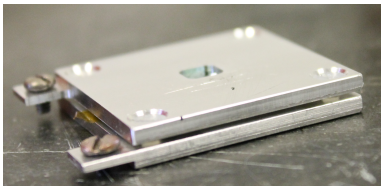

Figure V.8: **Air gate clamp** Custom clamp used to press the air gate and the graphene coated silicon nitride membranes. The clamp must be thin enough to fit within the cryostat and temperature stage and keep the sample at the proper working distance while enabling a bias to be applied between the two metal peices.

microns was the minimum distance between the gate and the sample to eliminate gate leaks.

Once we have the air gate and graphene on the silicon nitride membranes, the challenge remains on how to put them together. We do this with a custom clamp that pushes these two chips together and allows one to independently electrically contact both the gate and the graphene, see figure V.8.

V.6.3 Experimental Methods

In order to measure the profiles of the graphene sheets we collected data while applying different voltages between the gate and the graphene devices. Phase scanning mode (PSI) was used to extract the topography of the graphene while vertical scanning mode (VSI) was used to measure the distance between the gate and the graphene devices (details on PSI and VSI mode are in section II.3). Voltages were applied with a Keithly 2400 source meter, while ensuring that no current was leaking through the device. Temperature control was achieved with a liquid nitrogen cooled temperature stage with the sample in a nitrogen environment.

V.7 Experimental Findings

Figure V.9 shows a PSI image of a typical graphene device. When taking data in PSI mode, one does not collect data from holes without graphene. This mode is also useful for finding defects in the graphene sheet, which are readily apparent, as can be seen in the 20 micron hole above the 30 micron hole without graphene in figure V.9.

As a bias is applied between the graphene membrane and the air gate, the graphene deflects towards the air gate, as seen in figure V.10. This motion is non-hysteretic, indicating that the membranes are not slipping or breaking.

V.8 In-plane Stiffness of Graphene

The in-plane stiffness of graphene can be extracted from the change in height of the graphene membranes under bias using equation V.26. A fit of equation V.26 with data from a device is shown in figure V.11. The fitting parameters is M the in-plane stiffness, and η_0 the built-in stress.

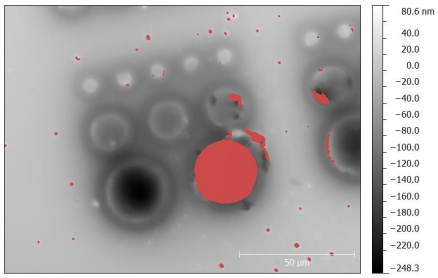

Figure V.9: **Graphene profile images** Interferometric image of graphene devices under 200 V. Note that the hole without graphene does not yield any data (hence its pink color)

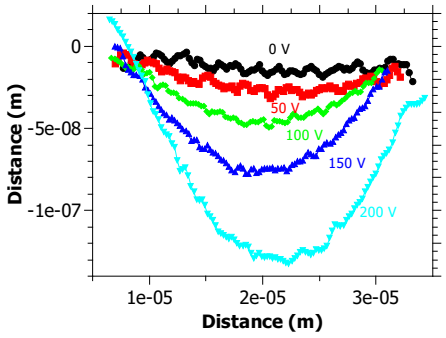

Figure V.10: **Graphene profiles** Graphene profiles of a 30 micron wide device at 0, 50, 100, 150 and 200 V.

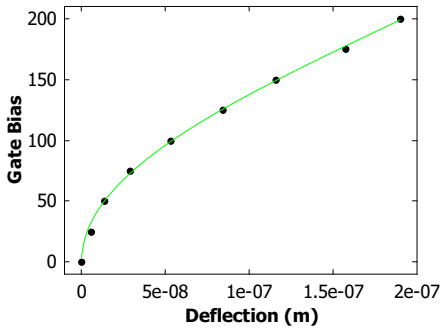

Figure V.11: **Center point deflection of graphene membrane** Points are the center point deflection of a graphene membrane versus gate voltage. The line is a fit to the data from the bulge test equations, enabling one to find both the strain and the in-plane stiffness of the membrane.

Annealing releases built in stress, with preannealed devices having stresses ranging from 0.2-0.09 N/m and the post annealed stress being 0.06-0.03 N/m. Prior to annealing extracting in-plane stiffness is more challenging and can only be done for devices with gate distances smaller than 30 microns. However, after annealing we get reasonable in-plane stiffness at room temperature. The two 30 micron membranes have an in-plane stiffness of $48 \pm 20 N/m$ and $50 \pm 40 N/m$. These low in-plane stiffnesses are much lower than the expected in-plane stiffness of 340 N/m expected from interatomic stretching in graphite.

The possible entropic nature of the in-plane stiffness is also manifest in its stress dependence, as each device has its natural built-in stress. This built-in stress could be due to several things, including self tensioning of the membrane on the sides of the holes[Bunch et al., 2008] and polymer resist on the membrane[Chen et al., 2009]. Annealing the sample changes the built-in stress, enabling one to explore a wider range of stress than allowed through electrostatic gating. Figure V.12 shows the in-plane stiffness of the devices that we measured versus the built-in strain. This data agrees with our simple model of a 2D entropic spring, dashed line in figure V.12.

A defining aspect of entropic springs is temperature dependence of their stiffness. This temperature dependence stiffness is also apparent in graphene. Figure V.13 shows graphene hardening as it is cooled, in qualitative agreement with equation V.26.

V.9 Conclusion

In conclusion, we observe a clear softening of the graphene in-plane stiffness. This softening may be due to the entropic nature of a two-dimensional sheet. With a room temperature in-plane stiffness of 50 N/m we measure graphene that is 7 times softer than graphite and previous large deflection measurements of graphene.

We see these results as transformative in the graphene mechanics literature as the in-plane stiffness of

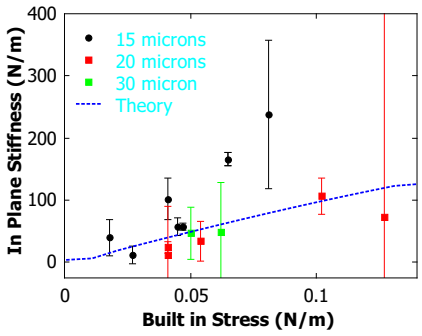

Figure V.12: **Stress versus in-plane stiffness** In-plane stiffness of graphene of 30, 20, and 15 micron graphene device. The dashed line is the expected inplane stiffness from section V.4.

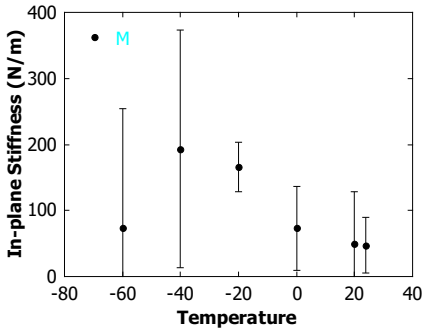

Figure V.13: **Temperature dependence of in-plane stiffness** A gradual stiffening of the membrane may be seen as this device is cooled, consistent with graphene as an entropic membrane.

graphite has generally been assumed for graphene devices. It also opens the window to tune the in-plane stiffness for graphene MEMS devices. However we see the greatest impact of this work as a new platform to study entropic effects, enabling researchers to move beyond the one dimensional model systems that have dominated the field.

CHAPTER VI

Conclusion

VI.1 Broader Impact

In conclusion, this dissertation demonstrates engineered strain in both graphene and MoS_2. The coefficient of thermal expansion of graphene has been measured with graphene in a bimetallic configuration. Bimetallic cantilevers also showed that there is a critical strain and temperature profile where graphene begins to slip along the substrate. This graphene substrate slipping puts an upper limit on strains that can be engineered in these systems and provides some of the first hints that flexural phonons are a dominate mechanism in these two dimensional materials.

By engineering strain in MoS_2 I was able to measure its Grüniesen parameter and extract how much its Raman spectra shifts with strain. I also showed that the band gap of MoS_2 is tunable with strain. More interestingly, the material was shown to transition from a direct bandgap to an indirect band gap material at 1.5% strain.

Finally I have shown that at low strains, graphene behaves like a two dimensional entropic spring, with an in-plane stiffness much less than traditional assumed for graphene. Following the theory for entropic membranes, the in-plane stiffness is shown to be temperature dependent.

VI.2 Future Work

VI.2.1 Non-uniform strain

In this document, either uniaxial or uniform strains are considered. While this have proven a fruitful enterprise, there are a host of interesting material properties that can be harnessed by exploring non-uniform strain.

In graphene, non uniform strain has been predicted to affect electron transport in a similar manner as a magnetic field. Signatures of 300 T pseudo-magnetic fields have been observed using scanning tunnelling microscopy[Levy et al., 2010] in strained graphene bubbles, but to date there has not been used to alter graphene's transport characteristics. By constructing a suspended graphene device one may be able to observe the pseudo quantum Hall effect.

Non-uniform strain engineering also has potential to alter dichalcolgenides in novel ways. With the knowledge that uniform strain can tune the band gap of these materials, non-uniform strain has the potential to created gradients of band gap. Gradients of band gap in these two dimensional materials enables one to transport charge neutral excitons, and has been proposed to create excitonic funnels and concentrators[Feng

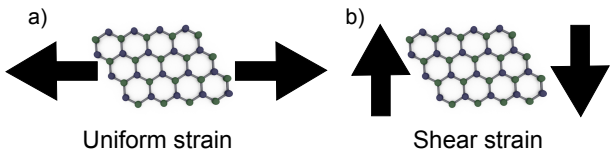

Figure VI.1: **Uniaxial and shear strain**. Uniaxial strain is generated by creating force as in part a) while shear strain is created by generating force as in b).

et al., 2012]. Even more exotically, by creating gradients of strain and hence, the bandgap, one can study exciton transport and create excitonic circuits.

VI.2.2 Shear Strain

Another avenue to explore controlling a two-dimensional material's properties is through shear strain. The uniform and uniaxial strain that is the focus of this document, forces are perpendicular to the graphene electrode interface. For shear strain the forces are parallel to this interface. Shear strains have the potential to create interesting rippling patterns in a two dimensional material and could be used to create one dimensional channels.

Creating shear strain is straightforward. Following the method outlines in section II.8 shear strain can be made by making suspended contacts where the gold contracts perpendicular to the graphene device as shown in figure VI.1.

VI.2.3 Graphene Cantilevers

In the work highlighted in chapter V, it was shown that the in-plane stiffness can be entropic in nature and can me much smaller than what has been assumed in the literature. Instead of stretching graphene in a membrane geometry, one can also bend graphene, as a cantilever for example. Unlike in-plane stiffness, where graphene behaves softer due to flexural phonons, the bending modulus is expected to be much higher than the calculated value of 1eV[Lu and Huang, 2009]. In light of this we have explored the fabrication of graphene cantilevers. Following the work of chapter V we can make graphene cantilevers by transferring graphene onto silicon nitride membranes and cutting out the graphene with an ion beam microscope.

We have not yet made a pure graphene cantilever that is stable in air, see figure VI.2. However by making a cantilever with a gold silicon nitride paddle at the end, we have managed to make cantilevers that can be measured in air, see figure VI.3.

We expect careful measurements of these devices to yield an acurate measure of graphene's bending modulus and enable a new route to probe the entropic mechanics of two dimensional materials.

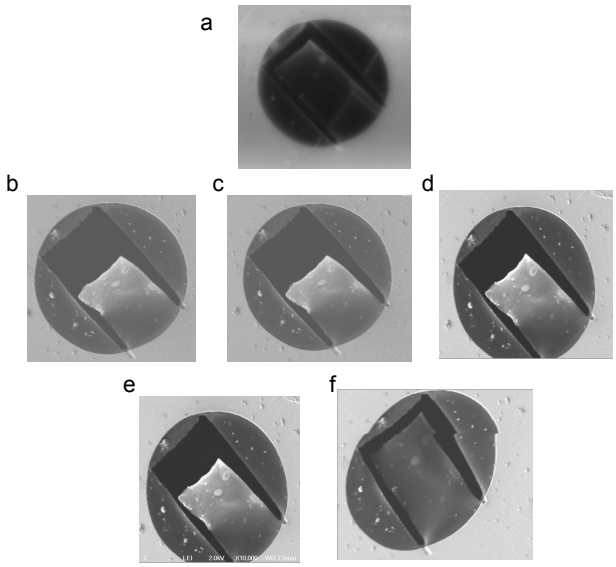

Figure VI.2: **Graphene Cantilever** a) Graphene cantilever cut out of a graphene membrane using a neon ion beam. Interestingly, the cantilever was not stable in air and crumples. b-f shows a progression of images of the cantilever when it was reloaded into a microscope, The cantilever unfurled itself. After being exposed to air the graphene again crumpled and did not unfurl in vacuum.

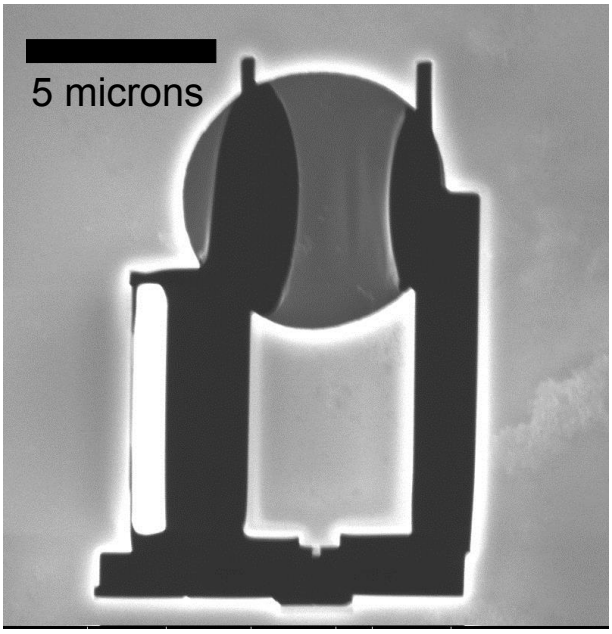

Figure VI.3: **Stable Graphene Cantilever** Instead of creating a pure graphene cantilever, it is possible to create a cantilever with a gold silicon nitride paddle. This paddle stabilized the cantilever and enables measurements of the cantilever with the interferometric profilometer.

VI.2.4 2D Bimetallic Cantilevers

Beyond the simple cantilevers shown in the previous section, it may be possible to create 2D bimaterial cantilevers. One can imagine a cantilever made from a layer of boron nitride on a layer of graphene. The possibility of these types of exotic cantilevers will allow one to both study mechanics and thermal properties on the atomic scale as well as adhesion between two dimensional materials.

VI.3 Conclusion

Mechanics of 2-D materials is a new field with rich physics that awaits exploration. By probing these materials we do not only learn about graphene or molybdenite or some other obscure compound, but we can gain insights about all two dimensional materials.

Appendix A

Graphene Resonators

One of the methods to determine strain in nanoscale devices highlighted in this dissertation is graphene mechanical resonators, see section II.4, enabling one to explore strain, and adsorbed mass. This section covers how to electrically measure a graphene mechanical resonator, shows some representative data, and shows how design of the nano-mechanical device strongly effects the temperature response of the device.

A.1 Electrical Measurement of Graphene Mechanical Resonator

All electrical measurements of a graphene mechanical resonator has been demonstrated by several groups [Chen et al., 2009; van der Zande et al., 2013; Xu et al., 2010]. For the work presented here we used a radio frequency detection with a vector network analyser[Xu et al., 2010].

Following the circuit diagram in figure A.1, a high frequency signal is sent from the vector network analyser (VNA) and combined with a DC offset using a bias tee. This combined signal actuates the graphene device. The DC part electrostatically pulls the sheet, while the RF component causes the sheet to vibrate. When the sheet is in motion a larger RF signal passes through the device and this is detected in the VNA.

Figure A.2 shows a typical data set from this setup. Mechanical resonances are tunable with strain and there are multiple resonances for a single devices. We assume that the lowest resonance is the fundamental resonance.

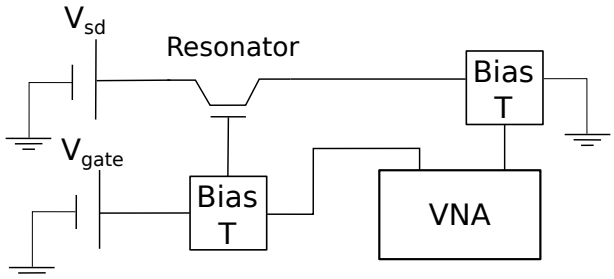

Figure A.1: **Circuit to measure mechanical resonance** This circuit is used to do direct readout of the mechanical resonance of a graphene mechanical resonator. A high frequency signal is sent through the gate and the return signal is measured with the Vector Network Analyser (VNA). DC bias to the source and the gate are applied through the bias T.

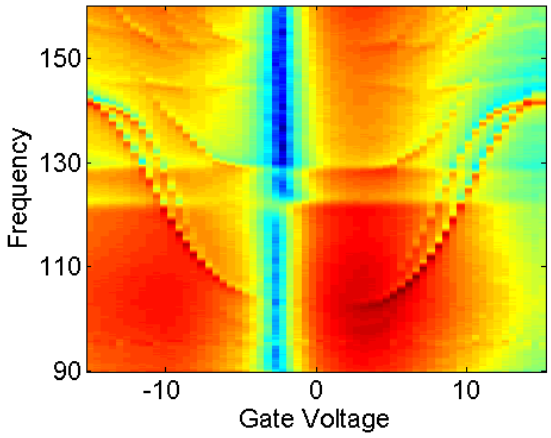

Figure A.2: **Mechanical resonance of graphene device** Mechanical resonance versus gate voltage for a suspended graphene device. Note that there are multiple mechanical resonances that are near each other in frequency, making it challenging to determine which resonance is the fundamental resonance

A.2 Strain versus temperature

We are able to track how strain changes for graphene mechanical resonator devices with temperature, see figure A.3. As the device cools down the resonance frequency increases, consistent with the device self tensioning while cooling. By fitting these curves to the equation II.19 one can extract the strain and the adsorbed mass on these devices as shown in figure A.4.

An interesting aspect of the strain versus temperature data is how different is is for different types of devices. There are two types of devices highlighted in figure A.4c. The red data where graphene is below the gold electrodes and the black data where graphene is above the gold electrodes. When graphene is below the gold electrodes the supporting silicon oxide is completely under etched leaving a long gold cantilever compared to when graphene is above the gold, see figure A.4a,b. These long gold cantilevers contract as the device cools down, straining the graphene device. By controlling the amount of gold that is cantilevered it is possible to control the strain in a low temperature graphene device.

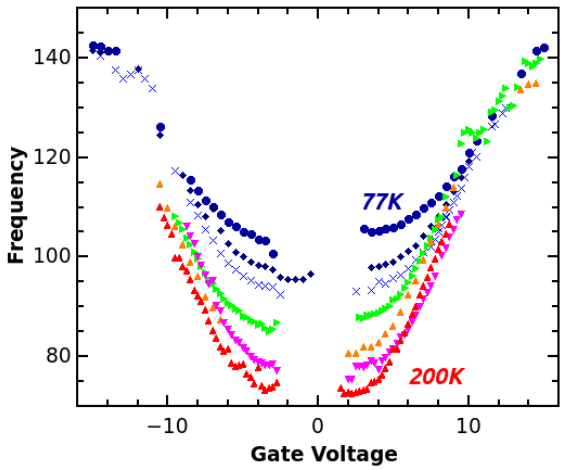

Figure A.3: **Temperature dependece of mechanical resonance of graphene device** Mechanical resonance of a single device as it cools down from 300 K to 77 K. The increase in resonant frequency is consistent with the device increasing in strain.

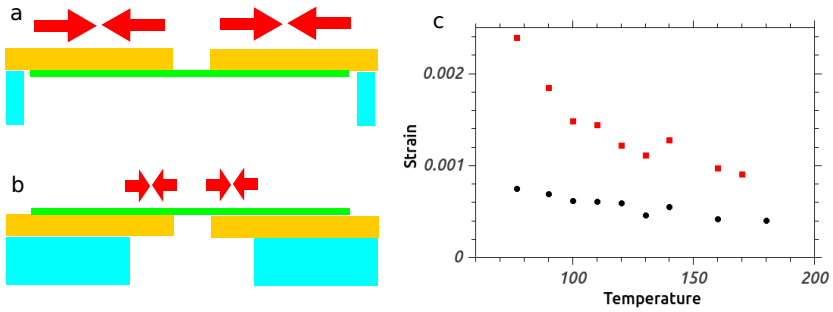

Figure A.4: **Strain versus temperature** We made two distinct types of graphene cantilevers, one with graphene on top, and the second with graphene underneath. a) As the device with graphene underneath cools down, the gold shrinks,causing the graphene to become strained. b) For the device with graphene on top the overhanging gold is much smaller and the graphene is not strained nearly as much with a change in temperature. c) Data from two different devices, one with graphene on top (black) and another with graphene underneath (red). The device with graphene underneath (red) is under much more strain at low temperatures as the device with graphene on top.

Appendix B

Thinnest Microfluidic Channels

Besides being the strongest, highest electron mobility, and thinnest material material ever measured, graphene can also make the thinnest microfluidic channels ever fabricated. By sandwiching graphene between a silicon oxide and a metal surface we can create a sub-nanometer channel that water can penetrate and propagate over several microns in distance.

The same physics that enables us to make sub-nanometer scaled microfluidic devices has been used for some time to etch silicon oxide underneath graphene. It has been observed that silicon oxide that is covered with graphene is preferentially etched in the presence of HF, a common silicon oxide etchant.

This behaviour is peculiar because normally when you cover a material something that is impermeable to an etchant, and graphene is impermeable to HF, you would expect it to act as an etch mask, protecting the material underneath from etching. Gold, for example, can be patterned on silicon oxide and the oxide under the gold remains unetched while the exposed oxide etches normally. Graphene, which is both not etched in HF and impermeable to HF[Bunch et al., 2008] would be expected to behave in the same manner. However when silicon oxide graphene-gold structures are etched, the silicon oxide under the graphene was etched at nearly the same rate as the exposed silicon oxide[Singh et al., 2010; Chen et al., 2009].

While the behaviour is clearly documented there is not clear model as to why silicon oxide is preferentially etched under graphene. I propose the hypothesis is that water and the HF disolved in the water are passively and rapidly transported along the graphene/silicon oxide interface. To probe this strange hypothesis two experiments were performed. First, we explored etch rates of silicon oxide along graphene versus etch rates into the oxide and second we probed how other materials besides HF can be transported along the graphene silicon-oxide interface.

B.1 Graphene assisted etching

To probe if water and HF are passively transported along the graphene/oxide interface we measure the etch rates of silicon oxide covered with graphene versus bare silicon oxide. This is done by covering graphene strips with gold. Gold by itself is a very effective etch mask for HF. Normally etching silicon oxide in the presence of gold will lead to the gold being undercut about the same distance as the etch depth, due to the isotropic nature of HF. However in the presence of graphene this is not the case. When there is a graphene stip under the gold the graphene aids in the etching of the oxide, as can be seen in figure B.2c.

We can see that while we only etch down 300 nm into the silicon oxide we etch more than 10 microns

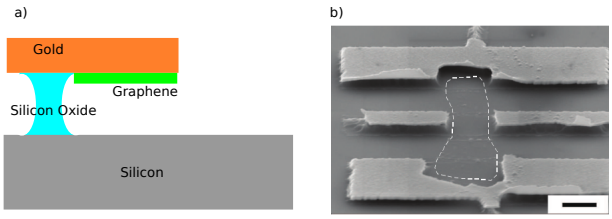

Figure B.1: **Silicon oxide etching in the presence of graphene** a) Schematic of graphene gold cantilever. The oxide under the graphene is etched despite being covered by gold, enabling us to make a graphene gold cantilever. b) SEM image of this type of etch. This was a silicon oxide, graphene, gold structure with graphene in the place of the the dashed white line. After removing the gold from the structure one can see how the silicon oxide is completely removed under the graphene. SEM image from supplement in reference [Singh et al., 2010].

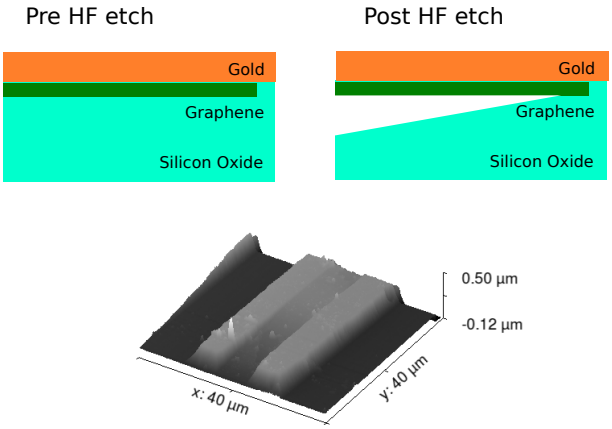

Figure B.2: **Anisotropic HF etching** While HF etching is normally isotropic, in the presence of HF in can become anisotropic, with a horizontal to vertical ratio of 80:1. a) Diagram of etch experiment before the etch. b) Diagram of graphene assisted etching. c) AFM image of an isotropic device after the removal of gold the show the etched silicon oxide.

horizontally along the graphene strip. This changes HF from being a normally isotropic etch with a 1:1 horizontal to vertical etch ratio to an anisotropic etchant with a 80:1 horizontal to vertical etch ratio. We suspect that water is passively transported in the interface and HF is carried along for the ride. In order to probe this hypothesis we explored how other small molecules are transported in the graphene/silicon oxide interface.

B.2 Water mediated transport of Rb and Eu salts under graphene

In order to confirm if HF is being actively transported along the graphene/silicon oxide interface, it is important to study the system in an environment where the silicon oxide is not being etched, so that we can decouple the etch from the transport of small molecules. We do this by performing the same style of study with Eu/Na and Rb/Na salts instead of HF. Time of flight secondary ion mass spectroscopy is used to detect

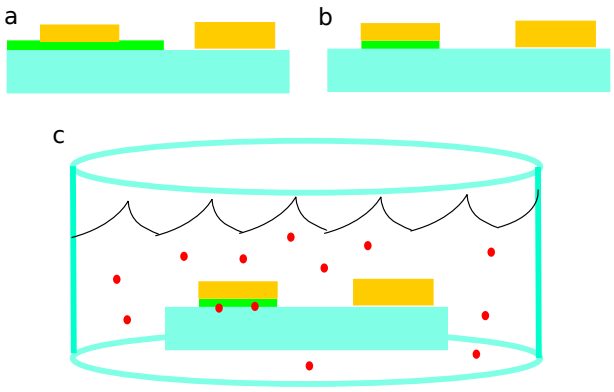

Figure B.3: **Fabrication of Eu and Rb transport devices** In order to make ultra-thin graphene mediated micro fluidic channels a) gold is patterned on a graphene silicon oxide substrate. b) Then the graphene is etched in an oxygen plasma. c) Finally the device is placed in a water bath with either an Europium or Rubidium salt.

the presence of these salts in the graphene silicon oxide interface.

B.2.1 Experimental setup

Devices were made by transferring CVD graphene onto a silicon oxide substrate. The CVD graphene in then patterned with gold islands. Then the device is etched in an oxygen plasma for 10 seconds to remove the graphene everywhere but under the gold islands, see figure B.3. If graphene can aid in transport of small molecules then one should find the salts under the gold islands and not under similar gold islands without a graphene between the gold and the silicon oxide. Unlike the case of HF, rare earth salts do not leave any clear optical trace. However the presence was determined using a time of flight secondary mass spectroscopy (TOF SIMS).

B.2.2 TOF SIMS

Time of flight secondary mass spectroscopy is a form of mass spectroscopy that enables one to probe the chemical content of nanoscale objects. The tool is basically a focused ion beam microscope with an attached time of flight mass spectrometer. This is a powerful combination. The focused ion beam allows one to image a particular place. As the location is imaged the ion beam mills away the substrate. The ejected particles are collected in the mass spectrometer. This enables one to probe the three dimensional chemical make-up of a nano-scale device. For example one can focus the beam in a narrow spot and extract a chemical depth profile as the beam drill into the sample.

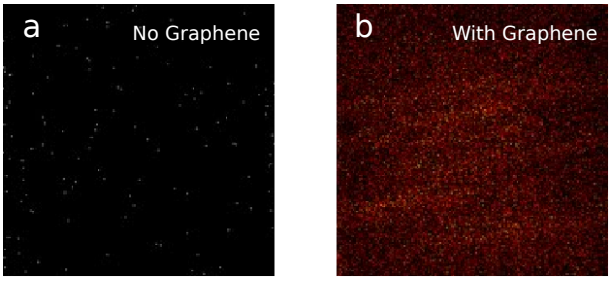

Figure B.4: **Europium transport with and without graphene** a) When there is no graphene between the chrome gold and the silicon oxide, no Europium is detected. b) However, with the presence of a graphene layer, the Europium is transported into this confined space.

B.2.3 Results

Figure B.4 contains an area map of Europium concentration under a gold square. We only find a significant concentration of Europium under the gold squares with graphene. Rb salts give a similar result. Not unsurprisingly, the Europium and Rubidium signals are too low in this two dimensional system in order to determine diffusion rates in this system.

B.3 Summery

In conclusion, we find two clear signatures that the graphene silicon oxide interface provides the thinnest possible microfluidic channel. First we see that on the interface of graphene and silicon oxide, HF anisotropically etches the oxide, etching along the graphene much faster than the oxide etch rate. This anisotropic etch rate indicates transport of water along the interface. This transport is confirmed using Rb and Eu salts and verifying that they are indeed transported along the graphene/silicon oxide interface.

BIBLIOGRAPHY

[Balandin et al., 2008] Balandin, A. a., Ghosh, S., Bao, W., Calizo, I., Teweldebrhan, D., Miao, F., and Lau, C. N. (2008). Superior thermal conductivity of single-layer graphene. *Nano letters*, 8(3):902–7.

[Bao et al., 2009] Bao, W., Miao, F., Chen, Z., Zhang, H., Jang, W., Dames, C., and Lau, C. (2009). Controlled ripple texturing of suspended graphene and ultrathin graphite membranes. *Nature Nanotechnology*, 4(9):562–566.

[Bao et al., 2012] Bao, W., Myhro, K., Zhao, Z., Chen, Z., Jang, W., Jing, L., Miao, F., Zhang, H., Dames, C., and Lau, C. N. (2012). In situ observation of electrostatic and thermal manipulation of suspended graphene membranes. *Nano letters*, 12(11):5470–4.

[Bertolazzi et al., 2011] Bertolazzi, S., Brivio, J., and Kis, A. (2011). Stretching and breaking of ultrathin MoS_2. *ACS Nano*, 5(12):9703–9.

[Blakslee et al., 1970] Blakslee, O., Proctor, D., Seldin, E., Spence, G., and Weng, T. (1970). Elastic constants of compression-annealed pyrolytic graphite. *Journal of Applied Physics*, 41(8):3373–3382.

[Bolotin et al., 2008] Bolotin, K., Sikes, K., Jiang, Z., Klima, M., Fudenberg, G., Hone, J., Kim, P., and Stormer, H. (2008). Ultrahigh electron mobility in suspended graphene. *Solid State Communications*, 146(9-10):351–355.

[Bunch et al., 2007] Bunch, J. S., van der Zande, A. M., Verbridge, S. S., Frank, I. W., Tanenbaum, D. M., Parpia, J. M., Craighead, H. G., and McEuen, P. L. (2007). Electromechanical resonators from graphene sheets. *Science (New York, N.Y.)*, 315(5811):490–3.

[Bunch et al., 2008] Bunch, J. S., Verbridge, S. S., Alden, J. S., van der Zande, A. M., Parpia, J. M., Craighead, H. G., and McEuen, P. L. (2008). Impermeable atomic membranes from graphene sheets. *Nano letters*, 8(8):2458–62.

[Cheiwchanchamnangij and Lambrecht,] Cheiwchanchamnangij, T. and Lambrecht, W. R. Quasiparticle band structure calculation of monolayer, bilayer, and bulk MoS_2. *Physical Review B*, (20):1–4.

[Chen, 2013] Chen, C. (2013). *Graphene NanoElectroMechanical Resonators and Oscillators*. PhD thesis, Columbia University.

[Chen et al., 2009] Chen, C., Rosenblatt, S., Bolotin, K. I., Kalb, W., Kim, P., Kymissis, I., Stormer, H. L., Heinz, T. F., and Hone, J. (2009). Performance of monolayer graphene nanomechanical resonators with electrical readout. *Nature Nanotechnology*, 4(12):861–7.

[Conley et al., 2011] Conley, H., Lavrik, N. V., Prasai, D., and Bolotin, K. I. (2011). Graphene Bimetallic-like Cantilevers: Probing Graphene/Substrate Interactions. *Nano letters*, 11(11):4748–52.

[Conley et al., 2013] Conley, H. J., Wang, B., Ziegler, J. I., Haglund, R. F., Pantelides, S. T., and Bolotin, K. I. (2013). Bandgap engineering of strained monolayer and bilayer MoS_2. *Nano letters*, 13(8):3626–30.

[de Andres et al., 2012] de Andres, P., Guinea, F., and Katsnelson, M. (2012). Bending modes, anharmonic effects, and thermal expansion coefficient in single-layer and multilayer graphene. *Physical Review B*, pages 1–5.

[Dikin et al., 2007] Dikin, D., Stankovich, S., Zimney, E., Piner, R., Dommett, G., Evmenenko, G., Nguyen, S., and Ruoff, R. (2007). Preparation and characterization of graphene oxide paper. *Nature*, 448(7152):457–460.

[Du et al., 2008] Du, X., Skachko, I., Barker, A., and Andrei, E. Y. (2008). Approaching ballistic transport in suspended graphene. *Nature nanotechnology*, 3(8):491–5.

[Feng et al., 2012] Feng, J., Qian, X., Huang, C., and Li, J. (2012). Strain-engineered artificial atom as a broad-spectrum solar energy funnel. *Nature Photonics*, 6(December):2–8.

[Guinea et al., 2009] Guinea, F., Katsnelson, M. I., and Geim, a. K. (2009). Energy gaps and a zero-field quantum Hall effect in graphene by strain engineering. *Nature Physics*, 6(1):30–33.

[Habermehl, 1998] Habermehl, S. (1998). Stress relaxation in si-rich silicon nitride thin films. *Journal of applied physics*, 83(9):4672–4677.

[He et al., 2013] He, K., Poole, C., Mak, K. F., and Shan, J. (2013). Experimental demonstration of continuous electronic structure tuning via strain in atomically thin mos_2. *Nano Letters*, 13(6):2931–2936.

[Helfrich and Servuss, 1984] Helfrich, W. and Servuss, R. (1984). Undulations, steric interaction and cohesion of fluid membranes. *Il Nuovo Cimento D*, 3(l).

[Huang et al., 2009] Huang, M., Yan, H., Chen, C., Song, D., Heinz, T. F., and Hone, J. (2009). Phonon softening and crystallographic orientation of strained graphene studied by Raman spectroscopy. *Proceedings of the National Academy of Sciences of the United States of America*, 106(18):7304–8.

[Jang et al., 2013] Jang, W., Bao, W., Jing, L., Lau, C. N., and Dames, C. (2013). Thermal conductivity of suspended few-layer graphene by a modified T-bridge method. *Applied Physics Letters*, 103(13):133102.

[Kern et al., 1999] Kern, G., Kresse, G., and Hafner, J. (1999). Ab initio calculation of the lattice dynamics and phase diagram of boron nitride. *Physical Review B*, 59(13):8551–8559.

[Koenig et al., 2011] Koenig, S. P., Boddeti, N. G., Dunn, M. L., and Bunch, J. S. (2011). Ultrastrong adhesion of graphene membranes. *Nature Nanotechnology*, 6(9):543–546.

[Lavrik et al., 2004] Lavrik, N. V., Sepaniak, M. J., and Datskos, P. G. (2004). Cantilever transducers as a platform for chemical and biological sensors. *Review of Scientific Instruments*, 75(7):2229–2253.

[Lee et al., 2008] Lee, C., Wei, X., Kysar, J. W., and Hone, J. (2008). Measurement of the elastic properties and intrinsic strength of monolayer graphene. *Science (New York, N.Y.)*, 321(5887):385–8.

[Lee et al., 2010] Lee, C., Yan, H., Brus, L., Heinz, T., Hone, J., and Ryu, S. (2010). Anomalous lattice vibrations of single-and few-layer MoS2. *ACS nano*, 4(5):2695–2700.

[Lee et al., 2012] Lee, J.-U., Yoon, D., and Cheong, H. (2012). Estimation of youngs modulus of graphene by raman spectroscopy. *Nano Letters*, 12(9):4444–4448.

[Lee et al., 2011] Lee, J.-U., Yoon, D., Kim, H., Lee, S. W., and Cheong, H. (2011). Thermal conductivity of suspended pristine graphene measured by Raman spectroscopy. *Physical Review B*, 83(8):081419.

[LeMieux et al., 2006] LeMieux, M. C., McConney, M. E., Lin, Y.-H., Singamaneni, S., Jiang, H., Bunning, T. J., and Tsukruk, V. V. (2006). Polymeric nanolayers as actuators for ultrasensitive thermal bimorphs. *Nano Letters*, 6(4):730–734.

[Levy et al., 2010] Levy, N., Burke, S. a., Meaker, K. L., Panlasigui, M., Zettl, a., Guinea, F., Castro Neto, a. H., and Crommie, M. F. (2010). Strain-induced pseudo-magnetic fields greater than 300 tesla in graphene nanobubbles. *Science (New York, N.Y.)*, 329(5991):544–7.

[Li et al., 2012] Li, H., Zhang, Q., Yap, C. C. R., Tay, B. K., Edwin, T. H. T., Olivier, A., and Baillargeat, D. (2012). From Bulk to Monolayer MoS2: Evolution of Raman Scattering. *Advanced Functional Materials*, 22(7):1385–1390.

[Li, 2012] Li, T. (2012). Ideal strength and phonon instability in single-layer mos_2. *Phys. Rev. B*, 85:235407.

[Li et al., 2009] Li, X., Cai, W., An, J., Kim, S., Nah, J., Yang, D., Piner, R., Velamakanni, A., Jung, I., Tutuc, E., Banerjee, S. K., Colombo, L., and Ruoff, R. S. (2009). Large-area synthesis of high-quality and uniform graphene films on copper foils. *Science (New York, N.Y.)*, 324(5932):1312–4.

[Lin et al., 2012] Lin, M.-W., Liu, L., Lan, Q., Tan, X., Dhindsa, K. S., Zeng, P., Naik, V. M., Cheng, M. M.-C., and Zhou, Z. (2012). Mobility enhancement and highly efficient gating of monolayer MoS 2 transistors with polymer electrolyte. *Journal of Physics D: Applied Physics*, 45(34):345102.

[Lindsay et al., 2010] Lindsay, L., Broido, D. a., and Mingo, N. (2010). Flexural phonons and thermal transport in graphene. *Physical Review B*, 82(11):115427.

[López-Polín and Gómez-Navarro, 2014] López-Polín, G. and Gómez-Navarro, C. (2014). Stiffening graphene by controlled defect creation. *arXiv preprint arXiv: ....*

[Lu et al., 2012] Lu, P., Wu, X., Guo, W., and Zeng, X. C. (2012). Strain-dependent electronic and magnetic properties of MoS(2) monolayer, bilayer, nanoribbons and nanotubes. *Physical chemistry chemical physics : PCCP*, 14(37):13035–40.

[Lu and Huang, 2009] Lu, Q. and Huang, R. (2009). Nonlinear Mechanics of Single-Atomic-Layer Graphene Sheets. *International Journal of Applied Mechanics*, 01(03):443–467.

[Luo and Nayak, 2007] Luo, Y. and Nayak, D. (2007). Strain-silicon cmos with dual-stressed film. US Patent 7,214,629.

[Mak et al., 2010] Mak, K., Lee, C., Hone, J., Shan, J., and Heinz, T. (2010). Atomically Thin MoS_2: A New Direct-Gap Semiconductor. *Physical Review Letters*, 105(13):2–5.

[Mak et al., 2013] Mak, K. F., He, K., Lee, C., Lee, G. H., Hone, J., Heinz, T. F., and Shan, J. (2013). Tightly bound trions in monolayer MoS_2. *Nature materials*, 12(3):207–11.

[Mak et al., 2012] Mak, K. F., He, K., Shan, J., and Heinz, T. F. (2012). Control of valley polarization in monolayer MoS_2 by optical helicity. *Nature Nanotechnology*, 7(June):494–498.

[Martyniuk et al., 2006] Martyniuk, M., Antoszewski, J., Musca, C. A., Dell, J. M., and Faraone, L. (2006). Environmental stability and cryogenic thermal cycling of low-temperature plasma-deposited silicon nitride thin films. *Journal of Applied Physics*, 99(5):053519.

[Metzger et al., 2010] Metzger, C., Rémi, S., Liu, M., Kusminskiy, S. V., Castro Neto, A. H., Swan, A. K., and Goldberg, B. B. (2010). Biaxial strain in graphene adhered to shallow depressions. *Nano letters*, 10(1):6–10.

[Mohiuddin et al., 2009] Mohiuddin, T., Lombardo, a., Nair, R., Bonetti, a., Savini, G., Jalil, R., Bonini, N., Basko, D., Galiotis, C., Marzari, N., Novoselov, K., Geim, a., and Ferrari, a. (2009). Uniaxial strain in graphene by Raman spectroscopy: G peak splitting, Grüneisen parameters, and sample orientation. *Physical Review B*, 79(20):1–8.

[Mounet and Marzari, 2005] Mounet, N. and Marzari, N. (2005). First-principles determination of the structural, vibrational and thermodynamic properties of diamond, graphite, and derivatives. *Physical Review B*, 71(20):1–14.

[Nelson and Peliti, 1987] Nelson, R. and Peliti, L. (1987). Fluctuations in membranes with and hexatic order. 48:1085–1092.

[Newaz et al., 2013] Newaz, A., Prasai, D., Ziegler, J., Caudel, D., Robinson, S., Jr., R. H., and Bolotin, K. (2013). Electrical control of optical properties of monolayer mos_2. *Solid State Communications*, 155(0):49 – 52.

[Nix and MacNair, 1941] Nix, F. and MacNair, D. (1941). The thermal expansion of pure metals: copper, gold, aluminum, nickel, and iron. *Physical Review*, 60:597–605.

[Novoselov et al., 2005] Novoselov, K. S., Jiang, D., Schedin, F., Booth, T. J., Khotkevich, V. V., Morozov, S. V., and Geim, A. K. (2005). Two-dimensional atomic crystals. *Proceedings of the National Academy of Sciences of the United States of America*, 102(30):10451–10453.

[Pan and Zhang, 2012] Pan, H. and Zhang, Y.-W. (2012). Tuning the electronic and magnetic properties of mos_2 nanoribbons by strain engineering. *The Journal of Physical Chemistry C*, 116(21):11752–11757.

[Paszkowicz et al., 2004] Paszkowicz, W., Minikayev, R., Piszora, P., Knapp, M., Bähtz, C., Recio, J. M., Marqués, M., Mori-Sánchez, P., Gerward, L., and Jiang, J. Z. (2004). Thermal expansion of spinel-type si_3n_4. *Phys. Rev. B*, 69(5):052103.

[Patil et al., 2005] Patil, L., Pandey, R., Bange, J. P., Gaikwad, S., and Gautam, D. (2005). Effect of deposition temperature on the chemical properties of thermally deposited silicon nitride films. *Optical Materials*, 27(4):663–670.

[Potts et al., 2011] Potts, J. R., Lee, S. H., Alam, T. M., An, J., Stoller, M. D., Piner, R. D., and Ruoff, R. S. (2011). Thermomechanical properties of chemically modified graphene/poly(methyl methacrylate) composites made by in situ polymerization. *Carbon*, 49(8):2615 – 2623.

[Radisavljevic et al., 2011] Radisavljevic, B., Radenovic, a., Brivio, J., Giacometti, V., and Kis, a. (2011). Single-layer MoS_2 transistors. *Nature Nanotechnology*, 6(3):147–50.

[Ramasubramaniam, 2012] Ramasubramaniam, A. (2012). Large excitonic effects in monolayers of molybdenum and tungsten dichalcogenides. *Phys. Rev. B*, 86:115409.

[Rice et al.,] Rice, C., Young, R. J., Zan, R., Bangert, U., Wolverson, D., Georgiou, T., Jalil, R., and Novoselov, K. S. Raman-scattering measurements and first-principles calculations of strain-induced phonon shifts in monolayer MoS_2. *Physical Review B*, (8):081307.

[Ross et al., 2013] Ross, J. S., Wu, S., Yu, H., Ghimire, N. J., Jones, A. M., Aivazian, G., Yan, J., Mandrus, D. G., Xiao, D., Yao, W., and Xu, X. (2013). Electrical control of neutral and charged excitons in a monolayer semiconductor. *Nature communications*, 4:1474.

[Sánchez-Pérez et al., 2011] Sánchez-Pérez, J. R., Boztug, C., Chen, F., Sudradjat, F. F., Paskiewicz, D. M., Jacobson, R. B., Lagally, M. G., and Paiella, R. (2011). Direct-bandgap light-emitting germanium in tensilely strained nanomembranes. *Proceedings of the National Academy of Sciences of the United States of America*, 108(47):18893–8.

[Sanjurjo et al., 1983] Sanjurjo, J. A., López-Cruz, E., Vogl, P., and Cardona, M. (1983). Dependence on volume of the phonon frequencies and the ir effective charges of several iii-v semiconductors. *Phys. Rev. B*, 28:4579–4584.

[Sazonova, 2006] Sazonova, V. (2006). *A tunable carbon nanotube resonator*. PhD thesis, Cornell University.

[Sazonova et al., 2004] Sazonova, V., Yaish, Y., Ustünel, H., Roundy, D., Arias, T. a., and McEuen, P. L. (2004). A tunable carbon nanotube electromechanical oscillator. *Nature*, 431(7006):284–7.

[Scalise et al., 2012] Scalise, E., Houssa, M., Pourtois, G., Afanas'ev, V., and Stesmans, A. (2012). Strain-induced semiconductor to metal transition in the two-dimensional honeycomb structure of mos_2. *Nano Research*, 5(1):43–48.

[Selg and Kink, 2003] Selg, M. and Kink, R. (2003). Temperature dependence of hot luminescence in solid xenon: theory and experiment. *Low Temperature Physics*, 29(9):862–865.

[Shi et al., 2013] Shi, H., Pan, H., Zhang, Y.-W., and Yakobson, B. I. (2013). Quasiparticle band structures and optical properties of strained monolayer mos_2 and ws_2. *Phys. Rev. B*, 87:155304.

[Shiri et al., 2008] Shiri, D., Kong, Y., Buin, A., and Anantram, M. P. (2008). Strain induced change of bandgap and effective mass in silicon nanowires. *Applied Physics Letters*, 93(7):073114.

[Singamaneni et al., 2008] Singamaneni, S., LeMieux, M., Lang, H., Gerber, C., Lam, Y., Zauscher, S., Datskos, P., Lavrik, N., Jiang, H., Naik, R., Bunning, T., and Tsukruk, V. (2008). Bimaterial microcantilevers as a hybrid sensing platform. *Advanced Materials*, 20(4):653–680.

[Singh et al., 2010] Singh, V., Sengupta, S., Solanki, H. S., Dhall, R., Allain, A., Dhara, S., Pant, P., and Deshmukh, M. M. (2010). Probing thermal expansion of graphene and modal dispersion at low-temperature using graphene nanoelectromechanical systems resonators. *Nanotechnology*, 21(16):165204.

[Splendiani et al., 2010] Splendiani, A., Sun, L., Zhang, Y., Li, T., Kim, J., Chim, C.-Y., Galli, G., and Wang, F. (2010). Emerging photoluminescence in monolayer MoS_2. *Nano Letters*, 10(4):1271–5.

[Sundaram et al., 2013] Sundaram, R. S., Engel, M., Lombardo, A., Krupke, R., Ferrari, A. C., Avouris, P., and Steiner, M. (2013). Electroluminescence in single layer mos_2. *Nano Letters*, 13(4):1416–1421.

[Temple-Boyer et al., 1998] Temple-Boyer, P., Rossi, C., Saint-Etienne, E., and Scheid, E. (1998). Residual stress in low pressure chemical vapor deposition sinx films deposited from silane and ammonia. *Journal of Vacuum Science & Technology A*, 16(4):2003–2007.

[Townsend et al., 1987] Townsend, P. H., Barnett, D. M., and Brunner, T. A. (1987). Elastic relationships in layered composite media with approximation for the case of thin films on a thick substrate. *Journal of Applied Physics*, 62(11):4438–4444.

[van der Zande et al., 2013] van der Zande, A. M., Huang, P. Y., Chenet, D. a., Berkelbach, T. C., You, Y., Lee, G.-H., Heinz, T. F., Reichman, D. R., Muller, D. a., and Hone, J. C. (2013). Grains and grain boundaries in highly crystalline monolayer molybdenum disulphide. *Nature materials*, 12(6):554–561.

[Vlassak and Nix, 1992] Vlassak, J. and Nix, W. (1992). A new bulge test technique for the determination of Young's modulus and Poisson's ratio of thin films. *Journal of Materials Research*, 94305(August).

[Vlassiouk et al., 2013] Vlassiouk, I., Fulvio, P., Meyer, H., Lavrik, N., Dai, S., Datskos, P., and Smirnov, S. (2013). Large scale atmospheric pressure chemical vapor deposition of graphene. *Carbon*, 54:58–67.

[Wang et al., 2013] Wang, G., Zhu, C., Liu, B., Marie, X., Feng, Q., Wu, X., Fan, H., Tan, P., Amand, T., and Urbaszek, B. (2013). Strain tuning of optical emission energy and polarization in monolayer and bilayer MoS_2. *arXiv preprint*, page arXiv:1306.3442.

[Wang et al., 2012] Wang, Q. H., Kalantar-Zadeh, K., Kis, A., Coleman, J. N., and Strano, M. S. (2012). Electronics and optoelectronics of two-dimensional transition metal dichalcogenides. *Nature Nanotechnology*, 7(11):699–712.

[Weaver et al., 1990] Weaver, W., Timoshenko, S., and Young, D. (1990). *Vibration Problems in Engineering*. A Wiley-Interscience publication. John Wiley & Sons.

[Wikipedia, 2014] Wikipedia (2014). Soft matter — Wikipedia, the free encyclopedia. [Online; accessed 7-March-2014].

[Wolf, 1996] Wolf, I. D. (1996). Micro-Raman spectroscopy to study local mechanical stress in silicon integrated circuits. *Semiconductor Science and Technology*, 11(2):139–154.

[Wu et al., 2004] Wu, C., Fang, W., and Yip, M. (2004). Measurement of Mechanical Properties of Thin Films Using Bulge Test. *sem-proceedings.com*, (1).

[Xu et al., 2010] Xu, Y., Chen, C., Deshpande, V. V., DiRenno, F. a., Gondarenko, A., Heinz, D. B., Liu, S., Kim, P., and Hone, J. (2010). Radio frequency electrical transduction of graphene mechanical resonators. *Applied Physics Letters*, 97(24):243111.

[Yin et al., 2012] Yin, Z., Li, H., Li, H., Jiang, L., Shi, Y., Sun, Y., and Lu, G. (2012). Single-layer MoS_2 phototransistors. *ACS Nano*, 6(1):74–80.

[Yue et al., 2012] Yue, Q., Kang, J., Shao, Z., Zhang, X., Chang, S., Wang, G., Qin, S., and Li, J. (2012). Mechanical and electronic properties of monolayer MoS_2 under elastic strain. *Physics Letters A*, 376(12-13):1166–1170.

[Zande et al., 2010] Zande, A. M. V. D., Barton, R. a., Alden, J. S., Ruiz-Vargas, C. S., Whitney, W. S., Pham, P. H. Q., Park, J., Parpia, J. M., Craighead, H. G., and McEuen, P. L. (2010). Large-Scale Arrays of Single-Layer Graphene Resonators. *Nano letters*, pages 4869–4873.

[Zeng et al., 2012] Zeng, H., Dai, J., Yao, W., Xiao, D., and Cui, X. (2012). Valley polarization in MoS_2 monolayers by optical pumping. *Nature Nanotechnology*, 7(8):490–3.